The link between water and ferric iron in Earth's lower mantle

Johannes Buchen[1,2,3]*, Olivia S. Pardo[2], Vasilije V. Dobrosavljevic[2], Wolfgang Sturhahn[2], Takayuki Ishii[1]†, Stella Chariton[4], Eran Greenberg[4]‡, Thomas S. Toellner[5] & Jennifer M. Jackson[2]

[1] Bayerisches Geoinstitut, Universität Bayreuth, Bayreuth, Germany

[2] Seismological Laboratory, California Institute of Technology, Pasadena, CA, USA

[3] Department of Earth Sciences, University of Oxford, Oxford, UK

[4] GSECARS, The University of Chicago, Chicago, IL, USA

[5] Advanced Photon Source, Argonne National Laboratory, Argonne, IL, USA

* Corresponding author. E-mail: johannes.buchen@uni-bayreuth.de

† Present address: Institute for Planetary Materials, Okayama University, Misasa, Japan

‡ Present address: Applied Physics Division, Soreq NRC, Yavne, Israel

Abstract

As the most massive geochemical reservoir, the lower mantle affects Earth's budget of volatile elements, including hydrogen or H_2O. The properties of minerals in Earth's lower mantle are further affected by changes in the electronic configurations of iron cations, i.e., spin transitions. Potential feedback between deep H_2O retention and spin transitions in mantle minerals, however, remain unexplored. We constrained the excess energy arising from the spin transition of ferric iron in high-pressure oxyhydroxide phases by a combination of high-pressure experiments. Our results show that the spin transition of ferric iron may stabilize oxyhydroxide phases in the lower mantle even at low H_2O concentrations. In addition, the spin transition expands the thermal stability of high-pressure oxyhydroxides and creates a geochemical link

between H_2O and ferric iron in Earth's lower mantle that might be sampled by rising plumes and reflected in related magmas produced at the surface.

Introduction

Basaltic magmas erupted at deep-rooted volcanic hotspots often contain more H_2O than magmas along mid-ocean ridges (*1, 2*). In some locations, elevated magmatic H_2O concentrations are further associated with high $Fe^{3+}/\Sigma Fe$ ratios (*3, 4*). These observations are commonly attributed to geochemical reservoirs that reside in Earth's lower mantle and are being sampled by rising plumes. In Earth's upper mantle, the availability and hence the thermodynamic activity of H_2O is controlled by the stability of minerals along geothermal gradients of different tectonic settings (*5-7*). Following subduction, hydrated rocks may sink deeper into the mantle and transport H_2O into the mantle transition zone and the uppermost lower mantle (*8-10*) where hydrated minerals of the transition zone are being replaced by dense hydrous magnesium silicates, such as superhydrous phase B and phase D, which remain stable to temperatures above those predicted for cold subduction pathways into the lower mantle (*9-12*).

Experiments at pressures above 30 GPa indicate that in the lower mantle H_2O might be retained in high-pressure oxyhydroxide phases such as $MgSiO_2(OH)_2$ (phase H) (*13, 14*) and δ-AlOOH (δ-phase) (*15, 16*). Solid solutions of these high-pressure oxyhydroxides coexist with Al-bearing bridgmanite in experiments resembling the pressures and temperatures of the lower mantle (*14, 17-20*). Similar to the system $MgSi_2O_4(OH)_2$–$Al_2SiO_4(OH)_2$ (phase D) (*12, 21*), the coupled substitution of Mg^{2+} and Si^{4+} by 2 Al^{3+} extends the stability of oxyhydroxide phases to higher pressures and temperatures, approaching expected temperatures of mantle geotherms with increasing pressure (*11, 13, 14, 17*). Assessing to which extent high-pressure

oxyhydroxide phases contribute to the H_2O budget of the lower mantle requires a detailed evaluation of their thermodynamic stability at pressures and temperatures of the lower mantle.

The dehydration temperatures and hence the stability limits of oxyhydroxide phases depend on the activity of H_2O in the respective chemical system. The H_2O activity, however, is hard to control in experiments, for example, because the H_2O component dissolves into a hydrous melt upon decomposition of oxyhydroxide phases (*13, 18, 19*). During dehydration experiments in diamond anvil cells using pressure-transmitting media such as neon (*16, 17*), the H_2O activity may be substantially reduced if H_2O is released from the sample material upon laser heating and lost to the pressure-transmitting medium. The reduced H_2O activity will then lead to lower dehydration temperatures. As an alternative to constraining dehydration temperatures by dehydration experiments, the relevant chemical equilibria may be evaluated based on the thermodynamic properties of the involved phases.

Oxyhydroxides in the lower mantle are expected to incorporate ferric iron (Fe^{3+}) when coexisting with Fe-bearing bridgmanite (*17, 18, 22*), with experiments showing that Fe-bearing oxyhydroxides undergo a spin transition at pressures between 30 and 40 GPa (*23-26*). Available information on the thermal stability and mineral chemistry of Fe-bearing oxyhydroxides indicates that these phases may remain stable to similar temperatures as their Fe-free counterparts while incorporating slightly more ferric iron than coexisting bridgmanite (*17, 18*). In view of the very limited H_2O storage capacities of ferropericlase (*27, 28*) and bridgmanite (*20, 27, 29, 30*), these factors suggest that the formation of an oxyhydroxide solid solution constitutes a feasible mechanism to retain H_2O in solid phases of the lower mantle. Indeed, oxyhydroxide phases are the only hydrous phases reported to remain stable at pressures in excess of about 50 GPa (*11, 13, 19*) and to coexist with bridgmanite in more complex chemical systems (*14, 17-20*). However, the impact of the spin transition of ferric iron on the

formation of high-pressure oxyhydroxide phases and hence on their ability to retain H_2O remains largely unexplored.

Results

Equation of state of δ-(Al,Fe)OOH

Assessing how the spin transition of ferric iron affects phase equilibria of high-pressure oxyhydroxides requires reliable measurements of thermodynamic properties as a function of pressure and temperature. We performed high-pressure powder X-ray diffraction experiments (XRD) on samples of δ-(Al,Fe)OOH with Fe/(Al+Fe) = 0.13 to determine the pressure-volume (*P*-*V*) relationship for this composition from 12 to 125 GPa at room temperature. In addition, we recorded powder XRD patterns at simultaneously high pressures and high temperatures by laser heating samples inside diamond anvil cells. From XRD patterns recorded at simultaneously high pressures and high temperatures, we derived the thermal pressures that resulted from heating δ-$Al_{0.87}Fe_{0.13}OOH$ to temperatures of up to 1580 K at high pressures. XRD patterns were analyzed by profile matching to extract unit cell volumes of δ-(Al,Fe)OOH and gold, which was used as a pressure calibrant. Examples of XRD patters recorded at high pressures and at simultaneously high pressures and high temperatures are shown in Figure 1 together with results of profile matching analyses. Further details of high-pressure XRD experiments and their analysis can be found in Materials and Methods.

The comparison of our room-temperature compression data with data of δ-(Al,Fe)OOH compounds with less (*23*) or no ferric iron (*16, 31*) clearly reveals a segment of enhanced volume reduction between 30 and 40 GPa (Fig. 2A) that has previously been identified and attributed to the spin transition of ferric iron in δ-(Al,Fe)OOH (*23, 26*). The transition of Fe^{3+} cations from the high-spin to the low-spin state leads to a reduction of the effective ionic radius

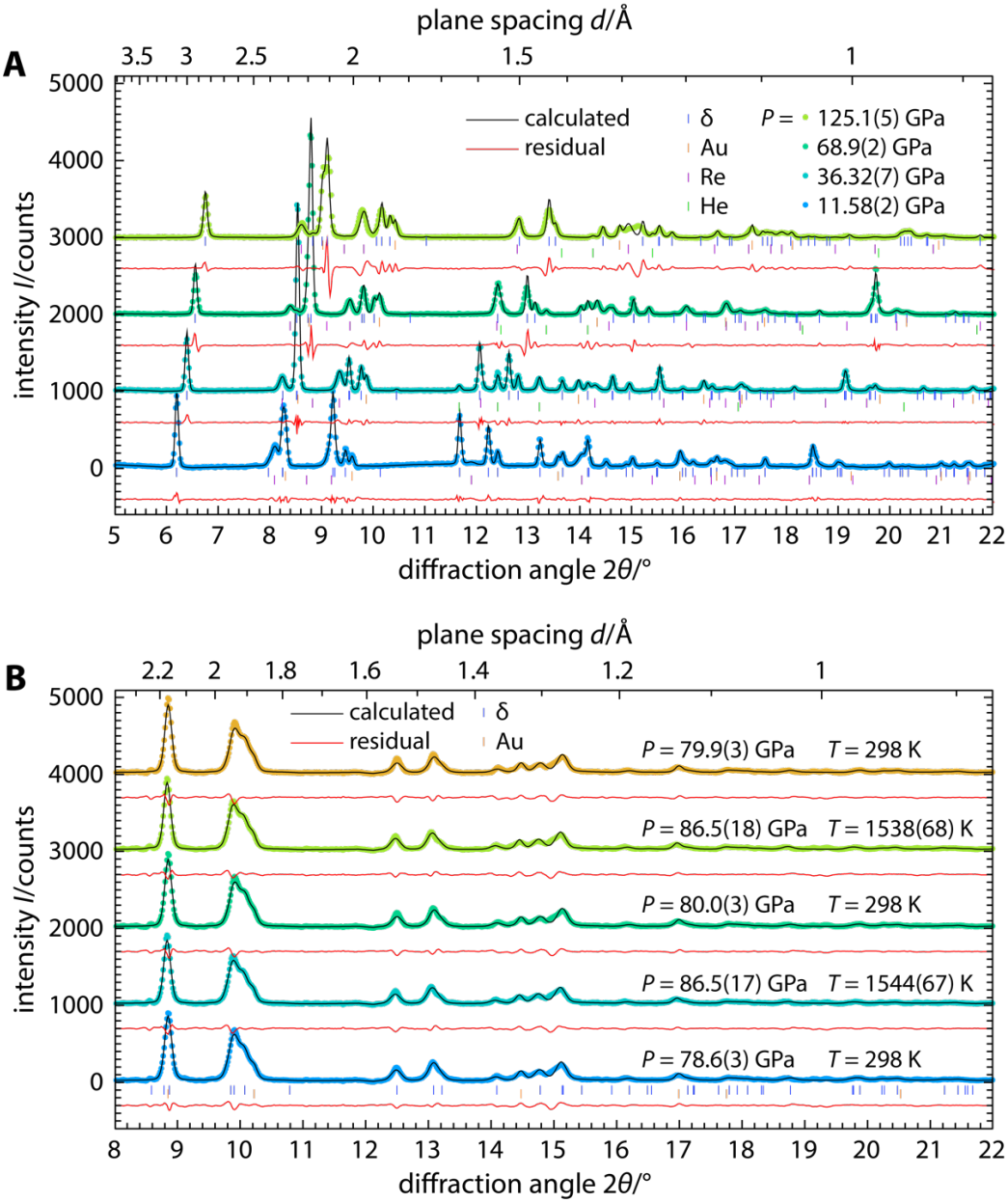

Fig. 1: Analysis of high-pressure X-ray diffraction patterns. (**A**) Examples of X-ray diffraction patterns recorded at different pressures and room temperature. (**B**) Example of a series of X-ray diffraction patterns recorded at simultaneously high pressures and high temperatures during a typical cycle of laser heating. X-ray diffraction patterns were corrected for background intensities and matched to calculated diffraction profiles by refining the lattice and peak shape parameters of δ-$Al_{0.87}Fe_{0.13}OOH$ (δ), gold (Au, pressure calibrant), rhenium (Re, gasket material, only in **A**), and helium (He, pressure-transmitting medium, only in **A**).

of Fe^{3+}. As a result, the unit cell volumes of δ-(Al,Fe)OOH with low-spin Fe^{3+} become similar to those of δ-AlOOH at pressures above 40 GPa.

We analyzed our *P*-*V* data with an equation of state (EOS) that accounts for the electronic excess pressure $P^{\#}$ due to the spin transition (Fig. 2A, Table 1). We describe the electronic excess pressure $P^{\#}$ in terms of a crystal-field model that allows to compute electronic excess contributions to the free energy and derived thermodynamic quantities such as pressure and bulk modulus (*32*). Since the spin transition broadens with increasing temperature, the impact on the compression curve is more prominent at room temperature than at high temperatures. The parameters for electronic excess contributions, however, are temperature-independent (Materials and Methods) and were therefore extracted from our room-temperature *P*-*V* data.

XRD patterns collected at combined high pressures and high temperatures were analyzed to derive pressure-volume-temperature (*P*-*V*-*T*) data for δ-(Al,Fe)OOH as well as for gold, which was compressed and heated simultaneously with the sample material. From the *P*-*V*-*T* datasets that resulted from multiple laser-heating cycles, we derived the thermal pressures acting on δ-(Al,Fe)OOH (Fig. 2B, Table S2; Materials and Methods). The thermal pressures were then combined with experimentally derived mean kinetic energies (see below) to constrain the parameters of a quasi-harmonic model that describes the vibrational and thermal properties of δ-(Al,Fe)OOH across the spin transition of ferric iron.

Vibrational properties and thermal EOS of δ-(Al,Fe)OOH

In addition to the effect on ionic radius, the spin transition modifies the Fe–O bonds and hence their vibrational frequencies. We collected nuclear resonant inelastic X-ray scattering (NRIXS) spectra up to 110 GPa (Fig. S3; Materials and Methods) to constrain changes in the spectrum of lattice vibrations that result from the changing electronic configuration of Fe^{3+} cations with increasing pressure. From the recorded NRIXS spectra, we derived projected

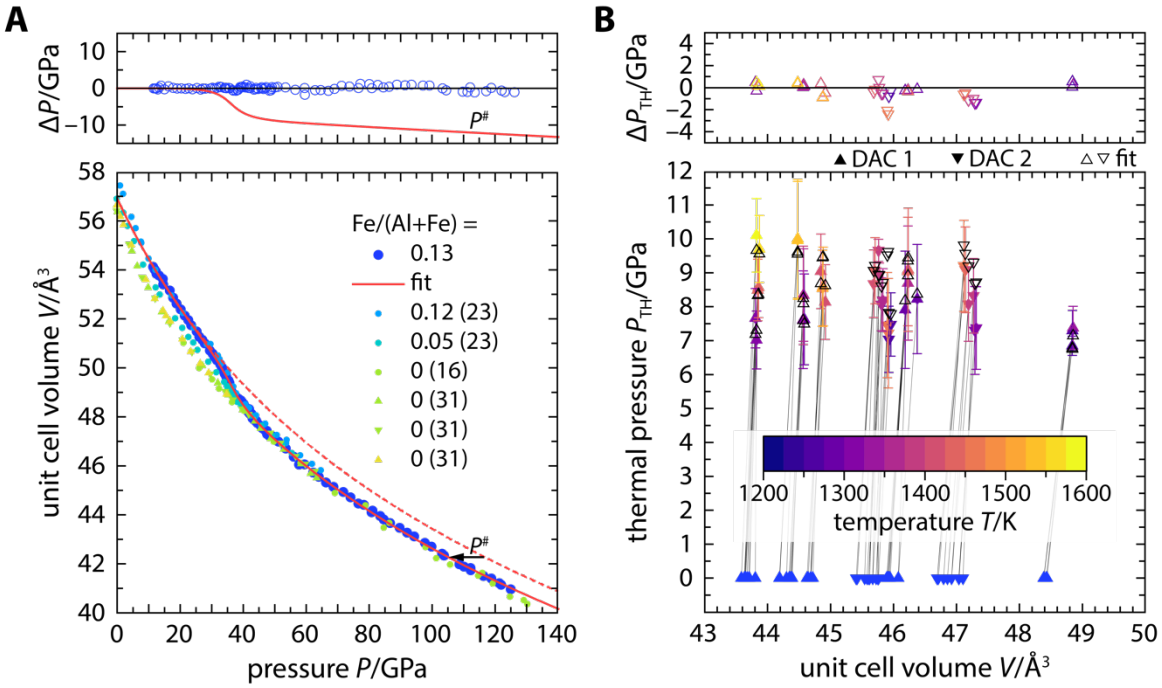

Fig. 2. Equation of state of δ-(Al,Fe)OOH. (**A**) Room-temperature compression data of δ-(Al,Fe)OOH with different iron contents. (**B**) Thermal pressures for δ-$Al_{0.87}Fe_{0.13}OOH$. The *P*-*V* data for δ-$Al_{0.87}Fe_{0.13}OOH$ in **A** and the thermal pressures in **B** were fit to an equation of state that accounts for excess contributions to pressure due to the spin transition of ferric iron. The effect of the electronic excess pressure $P^{\#}$ on the compression curve is indicated in **A**. The top panel in **A** shows the electronic excess pressure $P^{\#}$ along with fitting residuals. Tie lines in **B** connect data points of laser-heating cycles with room-temperature data shown in blue. The top panel in **B** shows fitting residuals of thermal pressures. In **A**, experimental uncertainties are within the sizes of the symbols. Error bars in **B** include propagated contributions from experimental uncertainties in volumes and temperatures.

partial phonon densities of states (p^3DOS) for vibrations of ^{57}Fe atoms in δ-(Al,Fe)OOH (Fig. 3A). When viewed together with p^3DOS for a similar composition with Fe/(Al+Fe) = 0.12 (*33*),

the p^3DOS show the typical rise of vibrational frequencies with compression as reflected in the shift of maxima in the p^3DOS to higher energies with increasing pressure.

At pressures around the spin transition (~40 GPa) (*23*), the p^3DOS changes more fundamentally as the main peak shifts abruptly to higher energies and broadens significantly. Similarly, other parts of the p^3DOS are affected by the spin transition. We note that changes in the vibrational structure caused by the spin transition of Fe^{3+} cations will be amplified in the p^3DOS as NRIXS selectively samples the vibrational motions of ^{57}Fe atoms. The Fe-selective character of NRIXS is therefore beneficial for resolving and quantifying changes in the spectrum of lattice vibrations caused by a spin transition of Fe atoms.

To condense the information content of the p^3DOS at high pressures, we computed the mean kinetic energy per vibrational mode and ^{57}Fe atom from each p^3DOS of δ-(Al,Fe)OOH with Fe/(Al+Fe) = 0.13 (this study) and 0.12 (*33*) and for simulated temperatures from 0 to 3300 K (Fig. 3B). Calculating kinetic energies at high temperatures ensures sampling of the entire energy range of the p^3DOS, including the high-energy portions, which are significantly less populated at room temperature. The derived mean kinetic energies reflect the changes in the p^3DOS caused by the spin transition of ferric iron in δ-(Al,Fe)OOH as well as how vibrational modes become populated with increasing temperatures.

The mean kinetic energies derived from the experimental p^3DOS were then used to constrain the parameters of a quasi-harmonic Debye model (*34*) for the FeOOH component of the δ-(Al,Fe)OOH solid solution. We assigned a separate Debye model to each spin state and calculated the population of spin states from the crystal-field model derived from our *P-V* data (see Materials and Methods). Our model captures the changes in mean kinetic energies across the spin transition as evidenced by low fitting residuals (Fig. 3B). The quasi-harmonic parameters of the AlOOH component were obtained by analyzing the thermal pressures derived from our high-pressure high-temperature XRD experiments (Fig. 2B) with a thermal EOS that

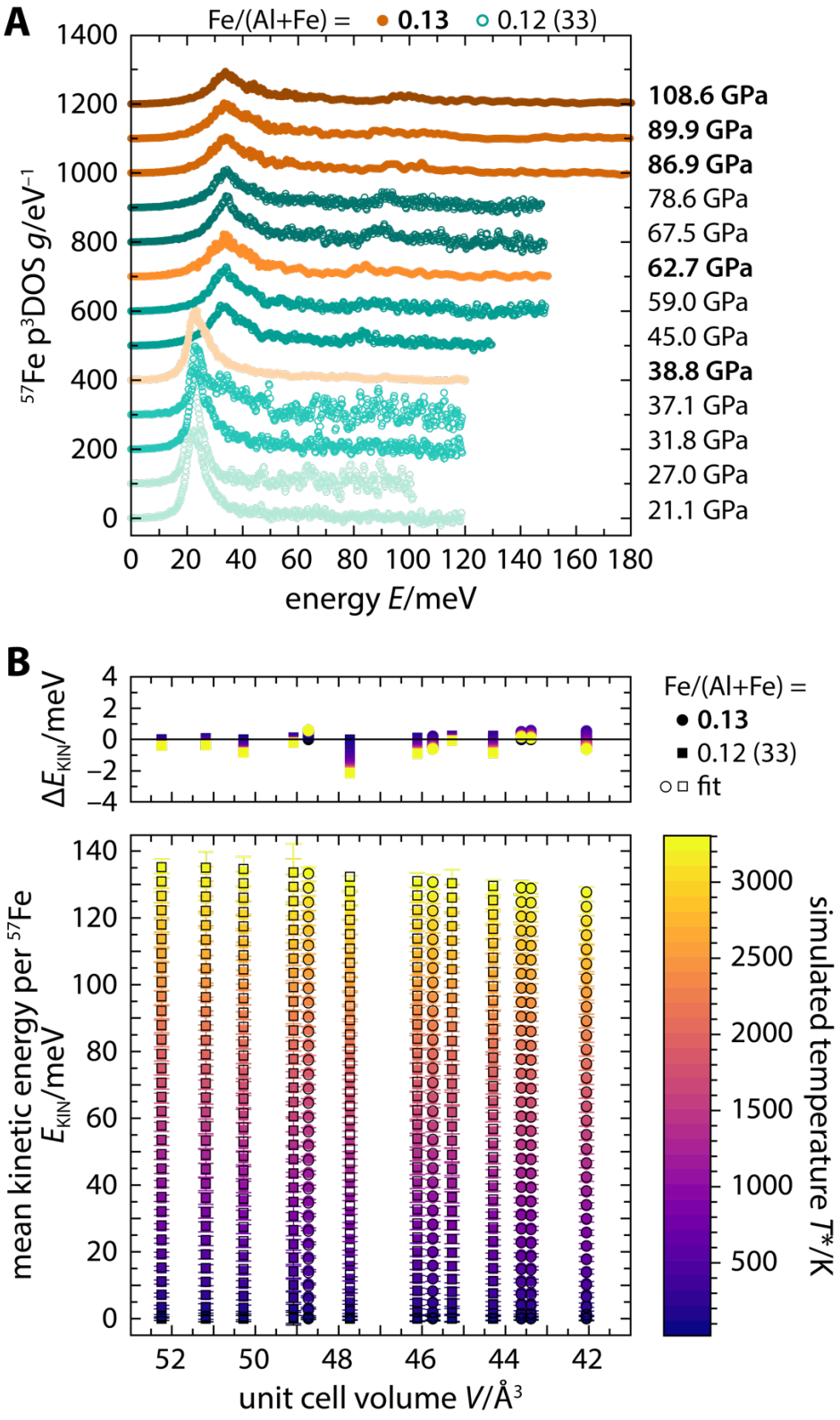

Fig. 3. Vibrational properties of δ-(Al,Fe)OOH at high pressures.

(see next page for full legend)

Fig. 3. Vibrational properties of δ-(Al,Fe)OOH at high pressures. (**A**) Projected partial phonon densities of states (p^3DOS) for ^{57}Fe atoms in δ-(Al,Fe)OOH at room temperature derived from NRIXS spectra. p^3DOS are vertically offset for clarity with the respective experimental pressures indicated on the right. (**B**) Mean kinetic energies of ^{57}Fe atoms in δ-(Al,Fe)OOH calculated directly from the p^3DOS in **A** and for a range of simulated temperatures T* (colored symbols). The mean kinetic energies in **B** were fit to a multi-state quasi-harmonic Debye model that accounts for changes in the vibrational spectrum caused by the spin transition of ferric iron (open squares and circles). The top panel in **B** shows fitting residuals. Error bars in **B** arise from propagating uncertainties on the p^3DOS.

describes the δ-(Al,Fe)OOH solid solution as a molar mixture of AlOOH and FeOOH components (Table 2; Materials and Methods).

Effect of the spin transition on phase equilibria with oxyhydroxide phases

As the result of our analysis of XRD and NRIXS data, we obtain a thermal EOS that accounts for changes in the electronic and vibrational energy due to the spin transition of ferric iron in δ-(Al,Fe)OOH. The underlying thermodynamic model and parameters can be used to compute excess contributions to thermodynamic quantities that arise from the spin transition. In the following, we apply our thermodynamic model to explore the impact of the spin transition of Fe^{3+} in high-pressure oxyhydroxide phases on the H_2O activity in Earth's lower mantle.

In experiments, bridgmanite and oxyhydroxide phases coexist with hydrous melts (*13, 14, 18-20*). The chemical equilibrium between the Fe-Al components of bridgmanite (bdm) and the oxyhydroxide phase (ohy) and the H_2O component of a coexisting melt or fluid phase (fl) can be formulated as:

201 $$FeAlO_3\ (bdm) + H_2O\ (fl) = FeAlO_2(OH)_2\ (ohy) \qquad (1)$$

202 In a rock in the lower mantle, the Fe-Al components will form solid solutions with other
203 bridgmanite and oxyhydroxide components such as the Mg-Si and Al-Al components, for
204 which analogous equilibria may be formulated. The equilibrium reaction (1) between the Fe-
205 Al components affects the overall H_2O activity as long as both phases incorporate an Fe-Al
206 component. Experiments on Fe-Al-bearing compositions and at relevant pressures and
207 temperatures have indeed observed the incorporation of an Fe-Al component both into
208 bridgmanite and the coexisting oxyhydroxide phase (*17, 18*).

209 For both mafic (*35*) and ultramafic (*36, 37*) bulk rock compositions, $FeAlO_3$ has been
210 identified as the predominant Fe^{3+}-bearing bridgmanite component with Fe^{3+} preferentially
211 occupying the larger dodecahedral site of the perovskite crystal structure and remaining in a
212 high-spin state up to the highest pressures of the lower mantle (*38-40*). Ferric iron in the high-
213 pressure oxyhydroxide phase, in contrast, undergoes a spin transition at about 35 GPa (*23, 24*).
214 The impact of this spin transition on reaction (1) can be evaluated by considering the reaction
215 energetics with and without the excess energy contributions arising from the spin transition.

216 If the spin transition changes the Gibbs free energy of the $FeAlO_2(OH)_2$ component by $\Delta^{\#}G$,
217 the ratio of the activities aH_2O of the H_2O component for a scenario with ($a^{\#}$) and without (a)
218 the spin transition is given by

219 $$\frac{a^{\#}\mathrm{H_2O}}{a\mathrm{H_2O}} = \frac{a_{\mathrm{bdm}}}{a^{\#}_{\mathrm{bdm}}}\frac{a^{\#}_{\mathrm{ohy}}}{a_{\mathrm{ohy}}}\exp\left(\frac{\Delta^{\#}G}{RT}\right) \qquad (2)$$

220 where the subscripts bdm and ohy identify the activities of the Fe-Al components in the
221 bridgmanite and oxyhydroxide solid solutions, respectively. Since Fe^{3+} does not partition
222 strongly between these phases (*17, 18*), we may assume that the activity ratios of the Fe-Al
223 components are close to unity and that the right-hand side of equation (2) is dominated by the
224 exponential term $\exp(\Delta^{\#}G/RT)$.

We computed the excess Gibbs free energy $\Delta^{\#}G$ arising from the spin transition using the thermodynamic model for δ-(Al,Fe)OOH derived from our experimental results. Using our model, we calculated the changes in the Gibbs free energy of the component $FeAlO_2(OH)_2$ that result from compression and heating to the pressures and temperatures of the lower mantle. By either allowing the populations of spin states to adopt their equilibrium values or by fixing them to their values at ambient condition, we obtain the changes in Gibbs free energy with and without the effect of the spin transition, respectively. The difference between both scenarios corresponds to the excess Gibbs free energy $\Delta^{\#}G$. Since our thermodynamic model can separate electronic and vibrational contributions, the excess Gibbs free energy $\Delta^{\#}G$ can be decomposed into several contributions as shown in Figure 4A.

If the Gibbs free energy of the component $FeAlO_2(OH)_2$ changes by $\Delta^{\#}G$ due to the spin transition, the equilibrium (1) may react in two ways, depending on whether the H_2O activity is buffered at a constant value or free to vary. The consequences of these two options are illustrated in Figure 4B. If the H_2O activity is free to vary, the relative change in H_2O activity brought about by the spin transition is given by the ratio of H_2O activities in equation (2). If the H_2O activity is buffered at a nearly constant value, for example, by a large volume of hydrous melt coexisting with bridgmanite and the oxyhydroxide phase, the equilibrium (1) will shift to higher temperatures by an amount $\Delta^{\#}T_{SOL}$ that depends primarily on the entropies of the $FeAlO_3$ component of bridgmanite and the H_2O component of the melt or fluid phase (Fig. 4B). We estimated the magnitudes of the potential effects of the spin transition of ferric iron in δ-(Al,Fe)OOH on reaction (1) as explained in detail in the Methods and Materials section.

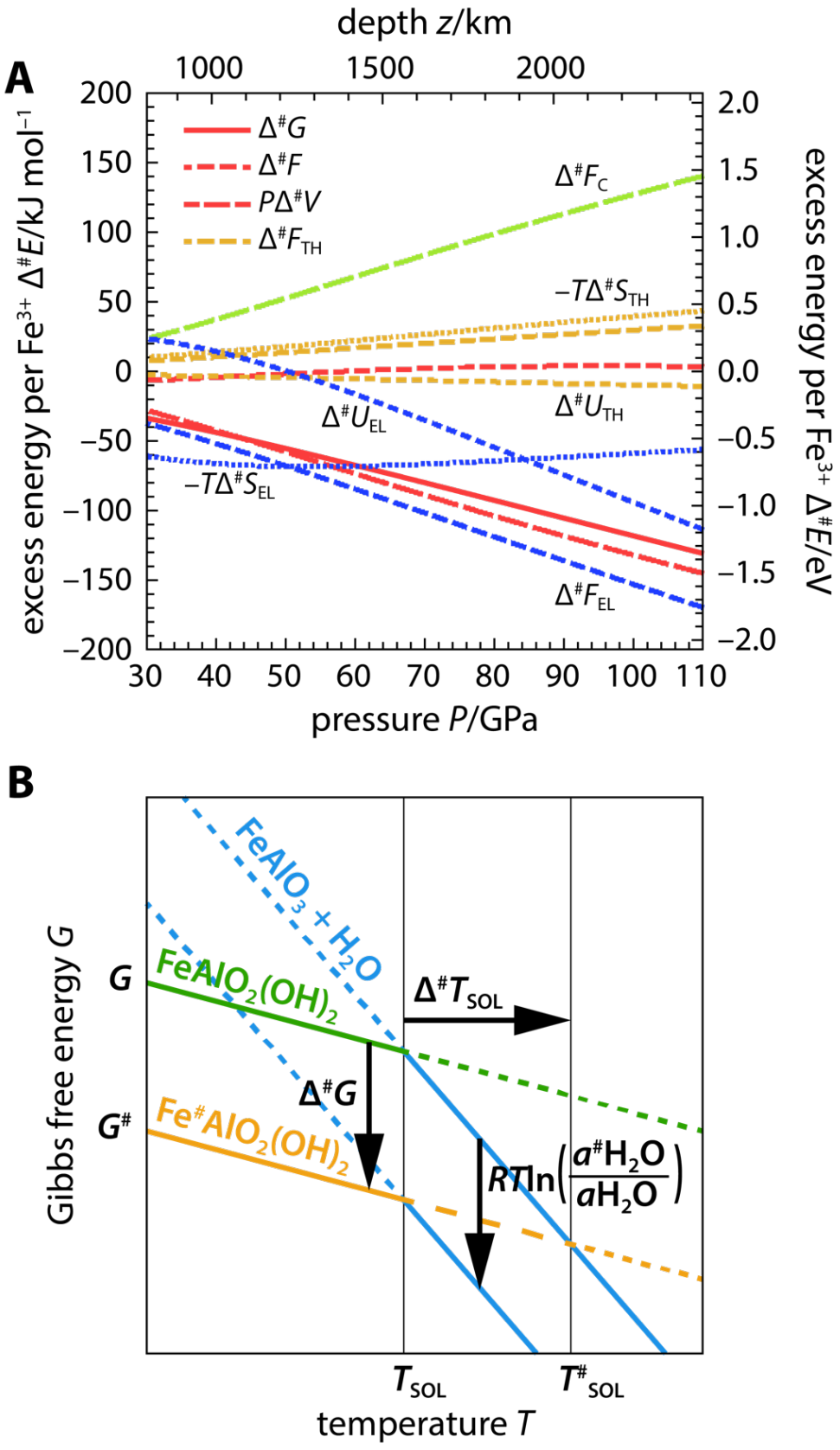

Fig. 4: Excess energy contributions arising from the spin transition of Fe^{3+} in high-pressure oxyhydroxides and the effect on phase equilibria. (see next page for full legend)

Fig. 4: Excess energy contributions arising from the spin transition of Fe^{3+} in high-pressure oxyhydroxides and the effect on phase equilibria. (**A**) Excess energy contributions along an isentropic temperature profile rooted at 25 GPa and 1400 K. Indices identify excess contributions to the cold (C), thermal (TH), or electronic (EL) parts of the Helmholtz free energy F, the internal energy U, and the entropy S. Excess contributions without indices refer to total contributions to the Gibbs free energy G, the Helmholtz free energy F, and volume work $P\Delta V$. (**B**) Schematic illustration of the effect of the spin transition on the phase equilibrium $FeAlO_3 + H_2O = FeAlO_2(OH)_2$. A reduction in Gibbs free energy of $\Delta^{\#}G$ by the spin transition of Fe^{3+} in $FeAlO_2(OH)_2$ can be compensated by reducing the water activity from $a H_2O$ to $a^{\#}H_2O$ or by raising the dehydration temperature T_{SOL} by $\Delta^{\#}T_{SOL}$.

Discussion

The relative change in H_2O activity brought about by the spin transition of ferric iron in a high-pressure oxyhydroxide phase can be calculated by evaluating the ratio $a^{\#}H_2O/aH_2O$ of equation (2) along isothermal and isentropic temperature profiles (*32*) through the lower mantle (Fig. 5A). Our modelling results suggest that the spin transition has the potential to decrease the activity of H_2O in a coexisting fluid phase in the lower mantle by several orders of magnitude. Along an isentropic temperature profile starting at 1900 K at 25 GPa, the H_2O activity would be reduced by a factor of 0.002 at a pressure of 100 GPa.

This strong reduction in H_2O activity also implies that an Fe^{3+}-bearing high-pressure oxyhydroxide phase may form at substantially lower H_2O concentrations if the effect of the spin transition is taken into account. Even if the amount of oxyhydroxide phase that forms at a given H_2O concentration might be minor in comparison to the amounts of major rock-forming minerals in the lower mantle, the H_2O activity may remain buffered at low levels as long as an Fe^{3+}-bearing oxyhydroxide phase contributes to the phase assemblage.

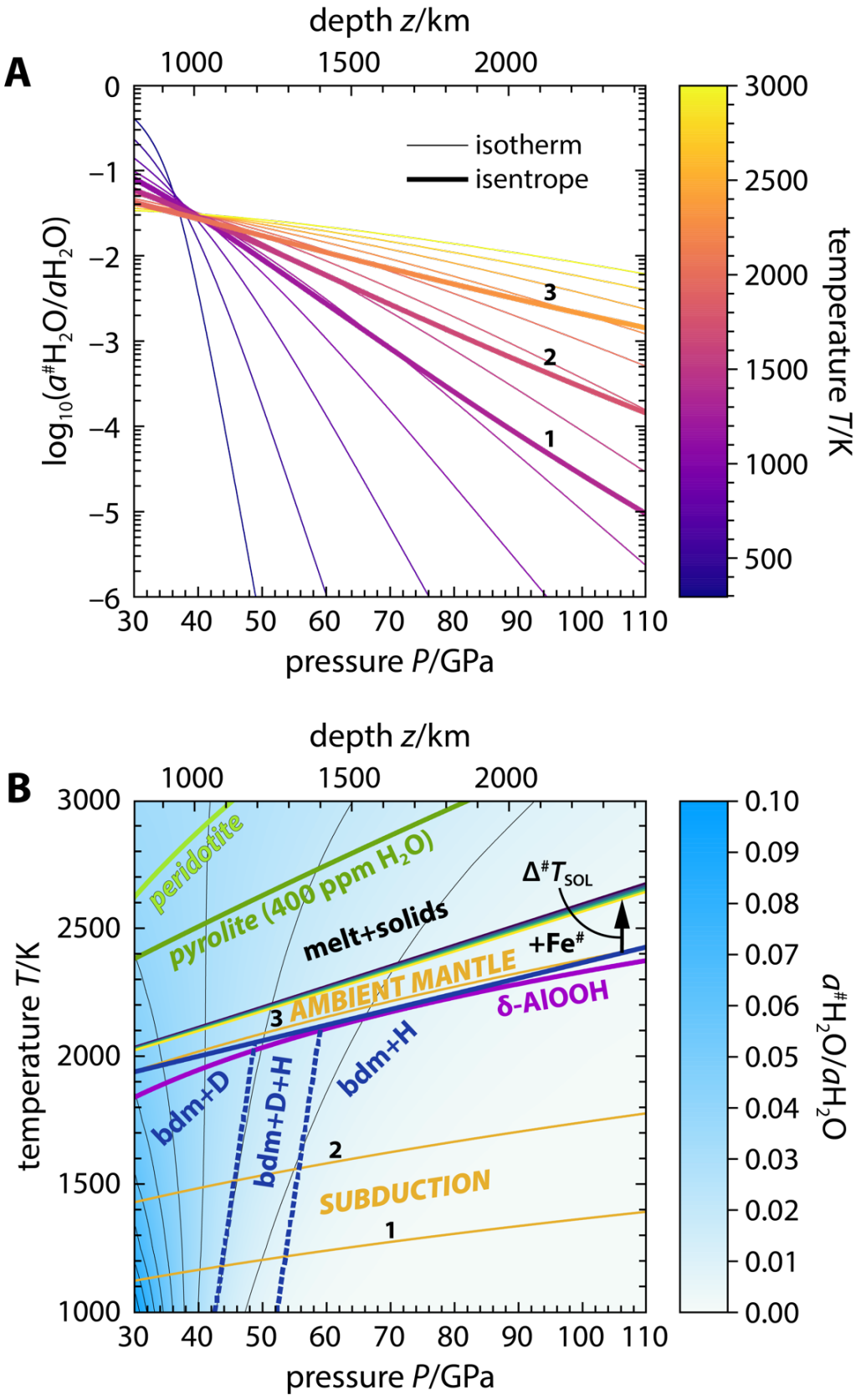

Fig. 5: Effect of the spin transition of Fe^{3+} in high-pressure oxyhydroxides on phase equilibria. (see next page for full legend)

Fig. 5: Effect of the spin transition of Fe^{3+} in high-pressure oxyhydroxides on phase equilibria. (**A**) Changes in H_2O activity, expressed as the ratio $a^{\#}H_2O/aH_2O$, brought about by the spin transition (#) along selected isothermal and isentropic temperature profiles. (**B**) Stability fields of high-pressure oxyhydroxide phases. Solidus curves are shown for δ-AlOOH (purple, (*16*)), $MgO–Al_2O_3–SiO_2–H_2O$ (blue, (*19*); bdm = bridgmanite, D = phase D, H = phase H), pyrolite with 400 wt-ppm H_2O (dark green, (*41*)), and peridotite (light green, (*42*)). The spin transition ($Fe^{\#}$) of Fe^{3+} in oxyhydroxides raises the solidus temperature by $\Delta^{\#}T_{SOL}$ (black arrow in **B**) if the H_2O activity is buffered at $aH_2O = 1$ (dark purple), 0.1, 0.01, 0.001, or 0.0001 (yellow). Isentropic temperature profiles marked 1, 2, and 3 in **A** and **B** start at 25 GPa and 1100 K, 1400 K, and 1900 K, respectively.

Although the exponential term in equation (2) indeed appears to dominate the H_2O activity ratio, the reduction of the H_2O activity may be modified by changes in the activity ratios of the Fe-Al components of bridgmanite and the oxyhydroxide solid solution. The magnitude of the effect on H_2O activity may be reduced if the $FeAlO_3$ component of bridgmanite underwent a spin transition. A spin transition of Fe^{3+} in the $FeAlO_3$ component of bridgmanite, however, is currently not supported by experimental or computational data (*38-40*) and would probably have a smaller effect on the molar volume of the $FeAlO_3$ component because Fe^{3+} and Al occupy different crystallographic sites in bridgmanite. Since the $P\Delta^{\#}V$ term dominates $\Delta^{\#}G$ (Fig. 4A) and Fe^{3+} and Al occupy a single crystallographic site in δ-(Al,Fe)OOH, a spin transition of Fe^{3+} can be expected to have a larger impact on the molar volume and hence on the excess Gibbs free energy of the Fe-Al component of an oxyhydroxide solid solution in comparison to bridgmanite.

While our model predicts the relative reduction in H_2O activity caused by the spin transition of Fe^{3+} in oxyhydroxides, absolute values of the H_2O activity in a coexisting melt phase may

be estimated based on existing thermodynamic models for the system MgO–SiO_2–H_2O (*10*). These models suggest H_2O activities on the order of 0.01 at pressures and temperatures where an oxyhydroxide phase replaces phase D. The spin transition of Fe^{3+} may then reduce the H_2O activity to values as low as 10^{-6} at 100 GPa along a subduction geotherm. At such low H_2O activities, the properties and behavior of the coexisting melt phase will approach those of an anhydrous silicate melt. For comparison, the molar fraction of H_2O in peridotitic source rocks of plume-derived magmas is on the order of 0.004 (750 wt-ppm H_2O, (*1, 2*)) and hence much higher in any partial melt formed from such rocks. The H_2O activities in partial melts of peridotitic rocks in the lower mantle therefore likely exceed the H_2O activities required to stabilize an Fe^{3+}-bearing oxyhydroxide phase in the lower mantle.

According to our thermodynamic analysis, an Fe^{3+}-bearing oxyhydroxide solid solution may form at H_2O activities substantially below those estimated for Fe-free compositions and hence at very low bulk H_2O concentrations. As a consequence, the H_2O activities and contents of melts in equilibrium with an Fe^{3+}-bearing oxyhydroxide phase may be lower than those required to significantly hydrate nominally anhydrous minerals of the lower mantle (*20, 27-30*). In this case, an Fe^{3+}-bearing oxyhydroxide phase would act as the main host for H_2O in solid phases of the lower mantle even if present only as a minor phase. As the effect of the spin transition on H_2O activities becomes stronger with increasing pressure, the formation of an Fe^{3+}-bearing oxyhydroxide phase is more favorable in the lowermost mantle than in the shallow lower mantle. Fe^{3+}-bearing oxyhydroxide phases may hence exert a stronger control on the H_2O budget of the lowermost mantle while H_2O might be released and partition into other phases in shallower parts of lower mantle.

If the H_2O activity in the fluid phase is buffered at a nearly constant value, the spin transition of ferric iron will stabilize oxyhydroxides to higher temperatures. This effect can be evaluated as the shift $\Delta^{\#}T_{SOL}$ of the dehydration reaction towards higher temperatures. Based on our

thermodynamic model for δ-(Al,Fe)OOH and thermodynamic data of bridgmanite and H_2O (Methods and Materials), we estimated the shift $\Delta^{\#}T_{SOL}$ along the solidus curve reported for the system $MgO–Al_2O_3–SiO_2–H_2O$ (*19*) and for different H_2O activities (Fig. 5B).

Since the solidus curve of the Fe-free system does not account for the effect of iron on dehydration temperatures and has been determined at unknown and probably varying H_2O activities (*19*), the exact location of the solidus curve for the Fe-bearing system cannot be obtained by simply adding the shift $\Delta^{\#}T_{SOL}$ to the experimentally observed solidus curve of the Fe-free system. For example, the replacement of Al by Fe^{3+} in δ-(Al,Fe)OOH may counteract the stabilizing effect of Al incorporation into oxyhydroxide phases (*13, 14, 19*). Instead, the magnitude of the shift $\Delta^{\#}T_{SOL}$ caused by the spin transition can be expected to be more meaningful than absolute dehydration temperatures.

As shown in Fig. 5B, the spin transition raises the temperature of the dehydration reaction by about 240 K for the pure component $FeAlO_2(OH)_2$ and may stabilize an Fe^{3+}-bearing oxyhydroxide phase in colder parts of the lower mantle and potentially even along typical geotherms for the ambient mantle. The magnitude of the effect varies only slightly with the H_2O activity in the coexisting fluid phase and remains almost unchanged for H_2O activities between 1 and 0.0001. Our results are consistent with the few available experimental data which suggest that at pressures above 90 GPa Fe-Al-bearing oxyhydroxides remain stable to temperatures well above 2000 K (*17*). Although the full effect applies to the pure component $FeAlO_2(OH)_2$, the spin transition of Fe^{3+} links the thermal stability of oxyhydroxides to their Fe^{3+} content with compositions richer in Fe^{3+} remaining stable to higher temperatures.

The stabilizing effect of ferric iron on high-pressure oxyhydroxides may be partially offset by spin transitions in other minerals. We note, however, that the spin state of ferric iron in bridgmanite, the main host for Fe^{3+} in the lower mantle (*36, 43*), remains controversial (*38-40, 44*). In experiments on Fe-free compositions (*13, 19*), a high-pressure oxyhydroxide phase

(phase H) replaces phase D only at pressures above 40 GPa. We anticipate that the presence of ferric iron will expand the field in which phase D and an oxyhydroxide phase coexist and that the spin transition of ferric iron in phase D (*45, 46*) may have a similar effect on H_2O activity and thermal stability as the here-proposed effect for the oxyhydroxide phase.

As mentioned throughout the discussion, our evaluation of the reaction between bridgmanite and H_2O to form an oxyhydroxide phase, or of the reverse reaction for dehydration, focuses on the effect of the spin transition of ferric iron in the oxyhydroxide phase. Other reactions and possibly spin transitions may affect this equilibrium, for example, by altering the activities of the Fe-Al components of bridgmanite and the oxyhydroxide solid solutions. A more comprehensive analysis of phase equilibria in the lower mantle involving hydrous phases, analogous to thermodynamic models for simpler systems (*10*), would require relevant thermodynamic data on all phases involved. While such data is not yet available, we demonstrate by our simplified analysis how spin transitions may influence phase equilibria and present a formalism that can be applied to integrate experimental data on spin transitions into thermodynamic models. While more data are needed to fully constrain the phase relations of oxyhydroxide phases at conditions of the lower mantle, our experimental data and analysis suggests a geochemical connection between ferric iron and H_2O in Earth's lower mantle.

H_2O may be transported from the Earth's surface into the deep mantle by slabs of cold and hydrated lithosphere (*9, 11*). In addition, hydrous rocks might have formed from the crystallization of a magma ocean and sequestered in the lower mantle (*47*). Some regions of the lowermost mantle, including large low shear-wave velocity provinces (LLSVP) and ultralow velocity zones (ULVZ), have been proposed to be enriched in iron (*48-50*). These regions might provide preferred sites for H_2O storage if their elevated iron concentrations raise the thermal stability of oxyhydroxide phases through the incorporation of ferric iron. Despite this potential association of oxyhydroxide phases with LLSVPs and ULVZs and compatible

seismic properties of Fe^{3+}-bearing oxyhydroxide phases (*33*), it is unlikely that the observed reductions in seismic wave speeds are caused by oxyhydroxide phases alone since their volume fraction will presumably be minor.

Plumes suggested to be rooted in the lowermost mantle (*48-50*), however, give rise to basaltic volcanism with systematically higher magmatic H_2O concentrations (*1, 2*) that correlate with high $Fe^{3+}/\Sigma Fe$ ratios (*3, 4*). Throughout Earth's history, the lower mantle may have acted as an H_2O reservoir with oxyhydroxide phases as an important host phase for H_2O in the lowermost mantle. Over time, the here-proposed geochemical affinity of H_2O to ferric iron, favored by the spin transition of ferric iron in high-pressure oxyhydroxide phases, may have resulted in the formation of a geochemical reservoir in the lowermost mantle which is probed by deep-rooted plume magmatism today and contributes to the association of high H_2O and high Fe^{3+} contents of related magmas (*1, 3, 4*).

Materials and Methods

Sample synthesis and composition

Crystals of δ-$Al_{0.87}Fe_{0.13}OOH$ were synthesized by heating a mixture of $Al(OH)_3$ and $^{57}Fe_2O_3$ powders in a multi-anvil press at 27 GPa and 1500 K. Details of the synthesis procedure and sample characterization have been published elsewhere (*51, 52*). To enhance the signal-to-noise ratio and to reduce collection times of high-pressure NRIXS spectra (see below), we used Fe_2O_3 powder enriched with the Mössbauer-active isotope ^{57}Fe to $^{57}Fe/\Sigma Fe$ = 96 %. The composition of eight δ-$Al_{0.87}Fe_{0.13}OOH$ grains was determined by electron microprobe analysis as Fe/(Al+Fe) = 0.13(2) (*52*). All samples used in this study were taken from the same synthesis batch.

High-pressure X-ray diffraction experiments

Grains of δ-$Al_{0.87}Fe_{0.13}OOH$ were repeatedly crushed between the tips of two diamond anvils to obtain a fine-grained powder. For high-pressure X-ray diffraction (XRD) experiments at room temperature, a flake of this powder was placed inside the pressure chamber of a symmetric diamond anvil cell (DAC) together with a ruby sphere and gold powder for pressure determination (*53, 54*). Pre-compressed helium was loaded as a pressure-transmitting medium.

For XRD experiments at combined high pressures and high temperatures, powder of δ-$Al_{0.87}Fe_{0.13}OOH$, a ruby sphere, and gold powder were sandwiched together between layers of $Al(OH)_3$ inside the pressure chambers of two symmetric DACs. In addition to preventing dehydration of the δ-$Al_{0.87}Fe_{0.13}OOH$ powder during heating cycles, the $Al(OH)_3$ layers served as pressures-transmitting medium and as thermal insulation. $Al(OH)_3$ undergoes partial amorphization under compression (*55*) and is not expected to absorb the radiation of the near-infrared laser used to heat the sample and gold powder. As a result, $Al(OH)_3$ did not contribute significantly to the recorded XRD patterns but effectively insulated the sample and gold powder from the diamond anvils during laser heating. All symmetric DACs were prepared using diamond anvils with 250-μm culets beveled to 300 μm. Pressure chambers were sealed with rhenium gaskets that were pre-indented to a thickness of 45 to 55 μm and drilled with an electric discharge machine. Photomicrographs of the pressure chambers of all three DACs loaded for XRD experiments are shown in Figure S1.

All high-pressure XRD patterns were collected at beamline 13-ID-D operated by GeoSoilEnviroCARS at the Advanced Photon Source at Argonne National Laboratory. The X-ray beam was focused to an area of 2.5 μm × 3.5 μm at the sample position and tuned to an energy of 37.078 keV (0.33438 Å). Diffracted X-rays were recorded on a Dectris Pilatus 1M CdTe detector. The detector distance and diffraction geometry were calibrated using a LaB_6 reference material. For high-pressure XRD experiments at room temperature, the DAC was

connected to an inflatable metallic membrane for remote pressure control. XRD patterns were collected with exposure times of 4 or 5 s. To increase the number of grains contributing to XRD patterns, the DAC was rotated about the vertical axis from –3° to +3° during each acquisition.

For XRD experiments at simultaneously high pressures and high temperatures, the sample and gold powder were heated inside the pressure chambers of DACs using the double-sided laser heating setup installed at beamline 13-ID-D. During laser heating, thermal emission spectra of the heated area were recorded through both diamond anvils and fit to gray-body emission curves using the software T-Rax ((*56, 57*); version 1.1, C. Prescher, 2016, www.github.com/CPrescher/T-Rax) to determine the temperature of the heated area. For a typical heating cycle, we first recorded an XRD pattern at room temperature with an exposure time of 5 s. We then irradiated the same area within the pressure chamber with the infrared lasers from both sides while recording another XRD pattern for 5 s. During the X-ray exposure, we collected a series of thermal emission spectra. After switching off the laser, we collected another XRD pattern at room temperature. The temperatures of subsequent heating cycles were adjusted by changing the laser output power. The temperature assigned to each high-temperature XRD pattern corresponds to the average temperature from all emission spectra collected during the acquisition of the XRD pattern at high temperature. The associated uncertainty was estimated as the standard deviation of the same set of temperatures.

Analysis of X-ray diffraction patterns

The images of XRD patterns as recorded by the area detector were read into the software DIOPTAS ((*58, 59*); versions 0.5.0 to 0.5.2, 2019–2020, www.github.com/Dioptas/Dioptas) and integrated to profiles of intensity as a function of the diffraction angle 2θ. Coherent stacks of diffraction profiles were then analyzed and corrected for common background intensities

using the program MINUTI ((*60*);version 2.2.1; W. Sturhahn, 2021, www.nrixs.com). Lattice parameters of δ-$Al_{0.87}Fe_{0.13}OOH$ and gold were extracted from the diffraction profiles by matching calculated profiles to the observed profiles using the software FullProf ((*61, 62*); version 2.6.2, 2020, www.ill.eu/sites/fullprof/index.html). For XRD patterns recorded at room temperature, additional reflections were attributed to rhenium and helium and included in the profile matching procedure. Examples of profile matching results are shown in Figure 1.

The unit cell volumes of gold, combined with temperatures for high-temperature XRD experiments, were used to calculate pressures from the EOS of gold (*53*) while uncertainties in unit cell volumes and temperatures were propagated into uncertainties on pressures. To calculate the thermal pressures P_{TH} acting on δ-$Al_{0.87}Fe_{0.13}OOH$, we paired each high-temperature (hot) P_H-V_H-T_H combination with the room-temperature (cold) P_C-V_C-T_C combination recorded immediately before or after the hot P_H-V_H-T_H combination and shifted the pair of pressures along the pressure axis to make the cold pressure P_C fall onto the room-temperature compression curve determined in helium. This procedure corrects for offsets in pressure caused by residual deviatoric stresses in the $Al(OH)_3$ pressure-transmitting medium while retaining any changes in pressure and volume caused by heating. The thermal pressure P_{TH} was then calculated by subtracting the cold pressure at the hot volume $P(V_H,T_C)$ as calculated from our room-temperature EOS from the corrected hot pressure P_H*, i.e., $P_{TH}(V_H,T_H) = P_H^*(V_H,T_H) - P(V_H,T_C)$, where T_C = 298 K. Unit cell volumes of δ-$Al_{0.87}Fe_{0.13}OOH$ and gold are compiled together with the respective (thermal) pressures and temperatures in Tables S1 and S2.

High-pressure nuclear resonant inelastic X-ray scattering experiments

Grains of δ-$Al_{0.87}Fe_{0.13}OOH$ were cleaved into smaller pieces with a razor blade and rinsed in acetone. A crystal fragment was placed inside the pressure chamber of a panoramic diamond

anvil cell (panDAC) together with a ruby sphere for pressure determination. Pre-compressed helium was loaded as a pressure-transmitting medium. For the panDAC, we used diamond anvils with 250-μm culets beveled to 300 μm. The pressure chamber was prepared from a beryllium disk pre-indented to a thickness of about 50 μm and drilled with an electric discharge machine. To further stabilize the beryllium gasket, we lined the pressure chamber with a mixture of boron powder and epoxy resin. Photomicrographs of the pressure chamber taken at different compression steps are shown in Figure S2.

After compression to about 20 GPa, we noted a contraction of the pressure chamber caused by lateral spreading of the boron-epoxy lining which may have resulted in (partial) loss of helium. As a result, the ruby sphere was enclosed between the sample and the boron-epoxy lining, which led to a deterioration of ruby spectra with increasing pressure. We therefore decided to determine pressures from Raman spectra of the diamond anvils (*63*) recorded with their culets in the focal plane of the optical setup. For consistency, we corrected pressures derived from ruby spectra (*54*) based on a cross-calibration between both pressure scales, which we established by measuring pressures on several other DACs, including another panDAC, with the same optical setup and using calibrations for both the ruby R_1 fluorescence line (*54*) and the Raman spectrum of diamond (*63*).

Nuclear resonant inelastic X-ray scattering (NRIXS) spectra were collected at beamline 3-ID-B of the Advanced Photon Source at Argonne National Laboratory. The X-ray beam was focused to about 15 μm × 15 μm at the sample position and irradiated the sample through one of the diamond anvils. The energy of incident X-ray photons was tuned around the resonance energy of ^{57}Fe (14.4 keV) with a bandwidth of about 1 meV using a high-resolution monochromator (*64*). To record NRIXS spectra, the X-ray energy was scanned across the resonance energy of ^{57}Fe in steps of 0.25 meV while recording time-delayed fluorescence photons for 2 to 5 s at each step using three avalanche photodiodes (APD). The APDs were

inserted into the radial apertures of the panDAC to detect fluorescence photons emitted by the sample after absorption events by ^{57}Fe atoms and transmitted through the beryllium gasket. The collection of a single NRIXS spectrum of adequate quality required scanning the relevant energy range 12 to 31 times. The recorded NRIXS spectra are shown in Figure S3.

Analysis of nuclear resonant inelastic X-ray scattering spectra

NRIXS spectra were compiled from sets of individual scans and processed using the software PHOENIX ((*65, 66*); version 3.0.4, W. Sturhahn, 2021, www.nrixs.com). After normalization, the projected partial phonon densities of states (p^3DOS) of the ^{57}Fe sublattice was extracted from each spectrum (*67, 68*). The p^3DOS describes the energy distribution of those lattice vibrations (phonons) that displace ^{57}Fe atoms from their equilibrium positions in the crystal structure of δ-$Al_{0.87}Fe_{0.13}OOH$. In addition, only displacements of ^{57}Fe atoms with a component along the X-ray wave vector contribute to the NRIXS spectrum. Since we used a crystal fragment in our high-pressure NRIXS experiments, we note that our NRIXS spectra might be affected by the vibrational anisotropy of ^{57}Fe atoms in δ-$Al_{0.87}Fe_{0.13}OOH$ (*52*). Given the consistency with an existing set of p^3DOS on a similar composition of δ-(Al,Fe)OOH (*33*) (Fig. 3A) and the unknown degree of anisotropy at high pressures, however, we assume that the p^3DOS extracted from our NRIXS spectra approximate the isotropic partial phonon densities of states reasonably well.

Isothermal equation of state of δ-$Al_{0.87}Fe_{0.13}OOH$

To evaluate how the spin transition of Fe^{3+} affects the stability of the δ-(Al,Fe)OOH component of oxyhydroxide phases, we need an equation of state (EOS) for δ-(Al,Fe)OOH that accounts for excess contributions to pressure due to the spin transition. A model for the electronic excess contributions to energy and pressure has recently been proposed for the

analysis of experimental results (*32*). Based on crystal-field theory, this model describes the free energy of the *d* electron shell of an iron cation in a specific electronic state *i* and in the limit of a strong octahedral crystal field as:

$$F_i = z_{i1}\Delta + z_{i2}B + z_{i3}C - kT\ln(m_i M_i) \quad (3)$$

The energy of a multi-electron state depends on the crystal-field splitting Δ and the Racah parameters *B* and *C* while the entropic term includes the spin multiplicity M_i and orbital degeneracy m_i of the multi-electron state. The coefficients z_{i1}, z_{i2}, and z_{i3} have been tabulated for each *d* electron configuration and multi-electron state (*69*). We further assume the crystal-field splitting Δ and the Racah parameters *B* and *C* to vary with volume as:

$$\Delta = \Delta_0 \left(\frac{V_0}{V}\right)^{\frac{\delta}{3}} \quad (4a)$$

$$B = B_0 \left(\frac{V_0}{V}\right)^{\frac{b}{3}} \quad (4b)$$

$$C = C_0 \left(\frac{V_0}{V}\right)^{\frac{c}{3}} \quad (4c)$$

with Δ_0, B_0, and C_0 being their respective values at ambient conditions. For a given volume and temperature, the excess free energy $F^{\#}(V,T)$ per iron cation that arises from redistributing electrons over different electronic states can then be expressed as:

$$F^{\#}(V,T) = \sum_i \Delta\varphi_i F_i + dkT \sum_i (\varphi_i \ln \varphi_i - \varphi_{i0} \ln \varphi_{i0}) \quad (5)$$

where $\Delta\varphi_i = \varphi_i(V,T) - \varphi_{i0}(V_0,T_0)$ is the change in the fraction $\varphi_i(V,T)$ of *d* electrons that occupy the electronic state *i* at the given volume and temperature with respect to the fraction $\varphi_{i0}(V_0,T_0)$ at ambient conditions, and *d* is the number of *d* electrons per iron cation. The fractions φ_i at thermal equilibrium can be found from the condition $(\partial F/\partial n_i)_{V,T,N} = 0$ for a micro-canonical ensemble with a total number of electrons *N* and $n_i = \varphi_i N$ (*32, 70*). In addition to the high-spin ($^6A_1$) and low-spin state ($^2T_2$), we include in our model a third state ($^4T_1$) with intermediate spin

multiplicity that is predicted to become populated by a significant fraction of Fe^{3+} cations at high temperatures (*32*). The excess contribution to pressure that arises from the spin transition then follows as $P^{\#} = -(\partial F^{\#}/\partial V)_T$.

For the equation of state $P(V,T)$, we then have:

$$P(V,T) = P_{\mathrm{C}}(V,T_0) + P^{\#}(V,T) + P_{\mathrm{QH}}(V,T) \quad (6)$$

with the isothermal (cold) contribution $P_{\mathrm{C}}(V,T_0)$, the electronic excess contribution $P^{\#}(V,T)$ due to the redistribution of *d* electrons (spin transition), and the quasi-harmonic contribution $P_{\mathrm{QH}}(V,T)$ due to lattice vibrations. Note that both the electronic excess contribution and the quasi-harmonic contribution will contribute to thermal pressures at $T > T_0$. All parameters of the electronic excess contribution, however, are temperature-independent and can be derived from room-temperature compression data.

By fitting experimental pressure-volume data, it is possible to constrain the parameters of the isothermal EOS, e.g., of a third-order Birch-Murnaghan EOS, in addition to some of the crystal-field parameters needed to evaluate the electronic excess energy. To fit our room-temperature compression data of δ-$Al_{0.87}Fe_{0.13}OOH$ (Fig. 2A, Table S1), we fixed the Racah parameters *B* and *C* at ambient conditions as well their ratio *C*/*B* to literature values derived from spectroscopic measurements (*71*), i.e., B = 655 cm^{-1} and C/B = 4.73. The exponent δ which describes the volume-scaling of the crystal-field splitting Δ is highly correlated with the corresponding exponent b (= c) for the Racah parameters and was therefore fixed to 5, the value for approximating the coordinating oxygens anions as point charges (*71*). All other isothermal EOS and crystal-field parameters were constrained by a least-squares fit to our compression data at room temperature and are summarized in Table 1.

574 Thermal equation of state of δ-$Al_{0.87}Fe_{0.13}OOH$

575 In addition to the electronic energy, the redistribution of *d* electrons over different electronic
576 states also changes the Fe–O bonds and hence the frequencies at which Fe atoms vibrate around
577 their positions in the crystal structure. This effect is clearly visible in the change of the shape
578 of the p^3DOS of ^{57}Fe atoms in δ-(Al,Fe)OOH at pressures around the spin transition of Fe^{3+}
579 (Fig. 3A). As with the electronic excess energy, the spin transition will therefore give rise to
580 an excess vibrational energy. Here, we will evaluate the effect of the spin transition on the
581 vibrational energy in terms of the mean kinetic energies E_{KIN} per ^{57}Fe atom that we calculated
582 from the experimental p^3DOS (Fig. 3A) for a temperature range from 0 to 3300 K (Fig. 3B).
583 Simulating kinetic energies at high temperatures aims at sampling the high-energy portions of
584 each p^3DOS that are less populated at room temperature. To translate the mean kinetic energies
585 derived from the p^3DOS into a form more compatible with existing formalisms of thermal
586 equations of state, we approximate the mean kinetic energies with a Debye model:

587 $$E_{\mathrm{KIN}} = \frac{3}{2} kT \left(\frac{T}{\theta_{\mathrm{Fe}}}\right)^3 \int_0^{\frac{\theta_{\mathrm{Fe}}}{T}} \frac{\tau^3}{e^{\tau} - 1} \mathrm{d}\tau \quad (7)$$

588 We account for the effect of the spin transition on mean kinetic energies by assigning a Debye
589 temperature θ_i to each electronic state and describe the Debye temperature θ_{Fe} of the Fe-bearing
590 substructure by their average weighted by the population of each electronic state:

591 $$\theta_{\mathrm{Fe}}(V,T) = \sum_i \varphi_i(V,T)\theta_i(V) \quad (8)$$

592 The Debye temperatures $\theta_i(V)$ are functions of volume, or finite strain, with parameters θ_{i0}, γ_{i0}
593 and q_{i0} (*34*). To constrain the quasi-harmonic parameters of the high-spin ($^6A_1$) and low-spin
594 states ($^2T_2$), we fit the multi-state Debye model described above to the mean kinetic energies
595 calculated from the p^3DOS (Fig. 3B). The populations of each state and at each pressure
596 (volume) were calculated from the crystal-field model we derived from the room-temperature
597 compression curve. Since a phase transition at around 10 GPa (*23, 33*) limits the pressure

598 interval over which the high-spin state dominates the vibrational structure, we had to fix some
599 of the respective quasi-harmonic parameters. Similarly, the third state ($^4T_1$) is not sufficiently
600 populated at room temperature. As a result, the vibrational properties of this state cannot be
601 sampled at room temperature and therefore do not contribute to the p^3DOS and kinetic energies
602 in Figure 3. In the following, we approximated the quasi-harmonic parameters of the
603 intermediate-spin state with the respective averages of the high-spin and low-spin states.

604 NRIXS selectively samples the vibrations of ^{57}Fe atoms and is therefore ideal for detecting
605 and quantifying changes in the vibrational structure across spin transitions. Transferring the
606 Fe-specific vibrational properties to the δ-(Al,Fe)OOH solid solution, however, requires
607 additional information on the thermal properties of the solid solution. The experimentally
608 observed thermal pressures (Fig. 2B) include contributions from both the Fe-bearing
609 substructure and the remainder of the crystal structure. To derive a thermal EOS for δ-
610 $Al_{0.87}Fe_{0.13}OOH$ and to incorporate our model for the vibrational structure of the Fe-bearing
611 substructure, we assume the Debye temperature of δ-$Al_{0.87}Fe_{0.13}OOH$ to be given by:

612 $$\theta(V,T) = x_{\mathrm{Fe}}\theta_{\mathrm{Fe}}(V,T) + (1 - x_{\mathrm{Fe}})\theta_{\delta}(V) \quad (9)$$

613 where x_{Fe} is the molar fraction of the FeOOH component and θ_δ is the Debye temperature of
614 the remainder of the oxyhydroxide solid solution, i.e., of the AlOOH component for δ-
615 (Al,Fe)OOH. The Debye temperature θ_δ follows a quasi-harmonic model (*34*) with parameters
616 $\theta_{\delta 0}$, $\gamma_{\delta 0}$ and $q_{\delta 0}$. The quasi-harmonic contribution to pressure is then given by:

617 $$P_{\mathrm{QH}}(V,T) = \frac{\gamma}{V}\Delta U_{\mathrm{QH}}(V,T) \quad (10)$$

618 The change in thermal energy ΔU_{QH} is calculated from a quasi-harmonic Debye model (*34, 72*)
619 and the Grüneisen parameter γ is given by the definition $\gamma = -\partial\ln\theta/\partial\ln V$. Note that the
620 additional rise in the Debye temperature across the spin transition will give rise to a positive
621 excursion of the Grüneisen parameter, enhancing the quasi-harmonic (or vibrational)
622 contribution to pressure and other properties as predicted by first-principles computations for

a spin transition in another material (*73*). Here, we constrained the quasi-harmonic parameters $\theta_{\delta 0}$, $\gamma_{\delta 0}$ and $q_{\delta 0}$ by fitting our model to the experimentally observed thermal pressures (Fig. 2B, Table S2) while keeping the quasi-harmonic parameters of the Fe-bearing substructure fixed. All quasi-harmonic parameters for the thermal EOS of δ-$Al_{0.87}Fe_{0.13}OOH$ are summarized in Table 2. The fact that the quasi-harmonic parameters we derived for the AlOOH component of δ-(Al,Fe)OOH are consistent with those of a thermal EOS for pure δ-AlOOH (*16*) (Table 2) corroborates our choice of partitioning contributions to the vibrational structure between the FeOOH and AlOOH components. However, we do not expect our model for the FeOOH component in the δ-(Al,Fe)OOH solid solution to describe the properties of the end member ε-FeOOH, for example, because the crystal-field model strictly applies to dilute systems.

Effect of ferric iron on the H_2O activity in Earth's lower mantle

For hydrous bulk rock compositions, such as hydrous mafic and ultramafic compositions, the activity of H_2O in Earth's lower mantle at pressures in excess of about 40 GPa will be linked to the reaction between the Fe-Al component of bridgmanite (bdm) and the H_2O component of a fluid or melt phase (fl) to form the Fe-Al component of an oxyhydroxide solid solution (ohy):

$$FeAlO_3\ (bdm) + H_2O\ (fl) = FeAlO_2(OH)_2\ (ohy) \qquad (11)$$

The reverse reaction describes the dehydration of Fe-bearing oxyhydroxides. All reactants are components of fluid or solid solutions with their chemical potentials given by:

$$\mu = \mu^* + RT \ln a \qquad (12)$$

where μ^* is the chemical potential, or Gibbs free energy, of the pure component and a is the activity of the component in solution. At thermodynamic equilibrium, the overall change in Gibbs free energy of reaction (11) equals zero, and we find for the activity of the H_2O component in a fluid phase:

$$a\mathrm{H_2O} = \frac{a_{\mathrm{ohy}}}{a_{\mathrm{bdm}}} \exp\left(\frac{\Delta^* G}{RT}\right) \qquad (13)$$

The subscripts ohy and bdm identify the Fe-Al components of the oxyhydroxide and bridgmanite solid solutions, respectively, and $\Delta^* G$ is the difference in Gibbs free energy between the pure components. To evaluate the effect of the spin transition of Fe^{3+} in the oxyhydroxide phase on reaction (11), we can calculate the H_2O activity with equation (13) for two scenarios: A) Fe^{3+} in the oxyhydroxide phase goes through a spin transition (marked with superscript #) and B) Fe^{3+} in the oxyhydroxide phase does not go through a spin transition, i.e., $\varphi(^6A_1) = 1$ and $\varphi(^2T_2) = \varphi(^4T_1) = 0$ at all pressures and temperatures. The ratio of the H_2O activities of both scenarios will then be given by:

$$\frac{a^{\#}\mathrm{H_2O}}{a\mathrm{H_2O}} = \frac{a_{\mathrm{bdm}}}{a^{\#}_{\mathrm{bdm}}} \frac{a^{\#}_{\mathrm{ohy}}}{a_{\mathrm{ohy}}} \exp\left(\frac{\Delta^{\#} G}{RT}\right) \qquad (14)$$

Here, $\Delta^{\#} G$ is the difference in Gibbs free energy between the Fe-Al component of the oxyhydroxide phase with and without a spin transition, i.e., $\Delta^{\#} G = \mu^{*\#}_{\mathrm{ohy}} - \mu^{*}_{\mathrm{ohy}}$, and can be calculated from our model for the electronic and vibrational excess contributions to energy, pressure, and entropy. Figure 4A shows energetic and entropic excess contributions to $\Delta^{\#} G$ along an isentropic temperature profile. Assuming that the activities of the Fe-Al components of bridgmanite and the oxyhydroxide phase, or their ratios, change only slightly, the right-hand side of equation (14) is dominated by the exponential term. Note that Fe^{3+} of the Fe-Al component of bridgmanite is expected to remain largely in the high-spin state (*38-40*) at pressures and temperatures of Earth's lower mantle.

Effect of ferric iron on the thermal stability of oxyhydroxides

The stability limit or dehydration of Fe-Al-bearing oxyhydroxides can be formulated as the reverse of reaction (11):

$$FeAlO_2(OH)_2\ (ohy) = FeAlO_3\ (bdm) + H_2O\ (fl) \qquad (12)$$

If the activity of H_2O in the fluid phase (fl) is buffered at a constant value, a reduction of the Gibbs free energy of the $FeAlO_2(OH)_2$ component of the oxyhydroxide phase by the spin

673 transition of Fe^{3+} will change the temperature for which reaction (12) is in equilibrium at a
674 given pressure, i.e, $\Delta G(P,T) = 0$. As illustrated in Figure 4B, the shift in temperature depends
675 on the reduction of the Gibbs free energy $\Delta^{\#}G$ due to the spin transition and on the slope
676 $(\partial G_{BP}/\partial T)_P = -S_{BP}$ of the breakdown products as $\Delta^{\#}T_{SOL} = \Delta^{\#}G/(\partial G_{BP}/\partial T)_P = -\Delta^{\#}G/S_{BP}$. In
677 fact, this approximation will slightly underestimate $\Delta^{\#}T_{SOL}$ because the entropy of the
678 $FeAlO_2(OH)_2$ component is neglected.

679 Assuming pure components $FeAlO_2(OH)_2$ and $FeAlO_3$ of the oxyhydroxide phase and
680 bridgmanite, respectively, the entropy S_{BP} of the breakdown products is given by the sum S_{BP}
681 $= S_{bdm} + S_{H2O} - R \ln(aH_2O)$, where R is the molar gas constant. The entropies S_{bdm} and S_{H2O} of
682 pure $FeAlO_3$ and H_2O, respectively, at the pressure and temperature of interest can be
683 calculated from thermodynamic data with the approximation that the entropy of the pure H_2O
684 component of a fluid phase or a melt is similar to the entropy of pure H_2O. For H_2O, we used
685 the same thermodynamic approach as in (*10*):

686 $$S = S^{\circ}_{298} + \int_{298}^{T} \frac{C^{\circ}(T)}{T}\,\mathrm{d}T \tag{13}$$

687 with tabulated parameters for the heat capacity $C^{\circ}(T)$ and the entropy S°_{298} at the reference
688 state (*10*). Due to the absence of relevant thermodynamic data on the bridgmanite component
689 $FeAlO_3$, we estimated the respective entropy by using a Debye model (*72*):

690 $$S = 9NR\left(\frac{T}{\theta}\right)^3 \int_0^{\frac{\theta}{T}} \frac{\tau^3}{e^{\tau}-1} - \tau^2 \ln(1-e^{-\tau})\,\mathrm{d}\tau \tag{14}$$

691 with a quasi-harmonic model for the Debye temperature θ of the bridgmanite component
692 $MgSiO_3$ (*34, 74*).

693 All properties ($\Delta^{\#}G$, S_{bdm}, S_{H2O}) were calculated along the solidus curve of the system MgO–
694 Al_2O_3–SiO_2–H_2O (*19*) to approximate the yet unknown solidus curve of the Fe-bearing system.
695 This approximation is justified by the observation that the incorporation of iron did not
696 significantly affect the solidus temperatures of phase D-bearing assemblages up to pressures of

32 GPa (*12*). Because the H_2O activity in fluid phases of experiments and in the mantle is unknown, we assumed a range of values aH_2O = 1, 0.1, 0.01, 0.001, and 0.0001. The estimated shift $\Delta^{\#}T_{SOL}$ was added to the solidus temperatures of the system $MgO–Al_2O_3–SiO_2–H_2O$ to illustrate how the spin transition of Fe^{3+} may stabilize oxyhydroxides to higher temperatures (Fig. 5B).

References

1. J. E. Dixon, L. Leist, C. Langmuir, J.-G. Schilling, Recycled dehydrated lithosphere observed in plume-influenced mid-ocean-ridge basalt. *Nature* **420**, 385-389 (2002). https://doi.org/10.1038/nature01215
2. M. M. Hirschmann, Water, melting, and the deep Earth H_2O cycle. *Annual Review of Earth and Planetary Sciences* **34**, 629-653 (2006). https://doi.org/10.1146/annurev.earth.34.031405.125211
3. M. Brounce, E. Stolper, J. Eiler, Redox variations in Mauna Kea lavas, the oxygen fugacity of the Hawaiian plume, and the role of volcanic gases in Earth's oxygenation. *Proceedings of the National Academy of Sciences U. S. A.* **114**, 8997-9002 (2017). https://doi.org/10.1073/pnas.1619527114
4. Y. Moussallam *et al.*, Mantle plumes are oxidised. *Earth and Planetary Science Letters* **527**, 115798 (2019). https://doi.org/10.1016/j.epsl.2019.115798
5. M. W. Schmidt, S. Poli, Experimentally based water budgets for dehydrating slabs and consequences for arc magma generation. *Earth and Planetary Science Letters* **163**, 361-379 (1998). https://doi.org/10.1016/S0012-821X(98)00142-3
6. D. H. Green, W. O. Hibberson, I. Kovacs, A. Rosenthal, Water and its influence on the lithosphere-asthenosphere boundary. *Nature* **467**, 448-451 (2010). https://doi.org/10.1038/nature09369
7. K. Mierdel, H. Keppler, J. R. Smyth, F. Langenhorst, Water solubility in aluminous orthopyroxene and the origin of Earth's asthenosphere. *Science* **315**, 364-368 (2007). https://doi.org/10.1126/science.1135422
8. B. Schmandt, S. D. Jacobsen, T. W. Becker, Z. Liu, K. G. Dueker, Dehydration melting at the top of the lower mantle. *Science* **344**, 1265-1268 (2014). https://doi.org/10.1126/science.1253358
9. E. Ohtani, K. Litasov, T. Hosoya, T. Kubo, T. Kondo, Water transport into the deep mantle and formation of a hydrous transition zone. *Physics of the Earth and Planetary Interiors* **143-144**, 255-269 (2004). https://doi.org/10.1016/j.pepi.2003.09.015
10. T. Komabayashi, S. Omori, Internally consistent thermodynamic data set for dense hydrous magnesium silicates up to 35 GPa, 1600°C: Implications for water circulation in the Earth's deep mantle. *Physics of the Earth and Planetary Interiors* **156**, 89-107 (2006). https://doi.org/10.1016/j.pepi.2006.02.002
11. E. Ohtani, Hydrous minerals and the storage of water in the deep mantle. *Chemical Geology* **418**, 6-15 (2015). https://doi.org/10.1016/j.chemgeo.2015.05.005
12. S. Ghosh, M. W. Schmidt, Melting of phase D in the lower mantle and implications for recycling and storage of H_2O in the deep mantle. *Geochimica et Cosmochimica Acta* **145**, 72-88 (2014). https://doi.org/10.1016/j.gca.2014.06.025

13. M. Nishi *et al.*, Stability of hydrous silicate at high pressures and water transport to the deep lower mantle. *Nature Geoscience* **7**, 224-227 (2014). https://doi.org/10.1038/ngeo2074
14. I. Ohira *et al.*, Stability of a hydrous δ-phase, AlOOH–$MgSiO_2(OH)_2$, and a mechanism for water transport into the base of lower mantle. *Earth and Planetary Science Letters* **401**, 12-17 (2014). https://doi.org/10.1016/j.epsl.2014.05.059
15. A. Sano *et al.*, Aluminous hydrous mineral δ-AlOOH as a carrier of hydrogen into the core-mantle boundary. *Geophysical Research Letters* **35**, L03303 (2008). https://doi.org/10.1029/2007gl031718
16. Y. Duan *et al.*, Phase stability and thermal equation of state of δ-AlOOH: Implication for water transportation to the Deep Lower Mantle. *Earth and Planetary Science Letters* **494**, 92-98 (2018). https://doi.org/10.1016/j.epsl.2018.05.003
17. H. Yuan *et al.*, Stability of Fe-bearing hydrous phases and element partitioning in the system MgO–Al_2O_3–Fe_2O_3–SiO_2–H_2O in Earth's lowermost mantle. *Earth and Planetary Science Letters* **524**, 115714 (2019). https://doi.org/10.1016/j.epsl.2019.115714
18. M. Nishi, T. Irifune, S. Gréaux, Y. Tange, Y. Higo, Phase transitions of serpentine in the lower mantle. *Physics of the Earth and Planetary Interiors* **245**, 52-58 (2015). https://doi.org/10.1016/j.pepi.2015.05.007
19. M. J. Walter *et al.*, The stability of hydrous silicates in Earth's lower mantle: Experimental constraints from the systems MgO–SiO_2–H_2O and MgO–Al_2O_3–SiO_2–H_2O. *Chemical Geology* **418**, 16-29 (2015). https://doi.org/10.1016/j.chemgeo.2015.05.001
20. T. Ishii, E. Ohtani, A. Shatskiy, Aluminum and hydrogen partitioning between bridgmanite and high-pressure hydrous phases: Implications for water storage in the lower mantle. *Earth and Planetary Science Letters* **583**, 117441 (2022). https://doi.org/10.1016/j.epsl.2022.117441
21. M. G. Pamato *et al.*, Lower-mantle water reservoir implied by the extreme stability of a hydrous aluminosilicate. *Nature Geoscience* **8**, 75-79 (2014). https://doi.org/10.1038/ngeo2306
22. M. Nishi, Y. Kuwayama, J. Tsuchiya, T. Tsuchiya, The pyrite-type high-pressure form of FeOOH. *Nature* **547**, 205-208 (2017). https://doi.org/10.1038/nature22823
23. I. Ohira *et al.*, Compressional behavior and spin state of δ-(Al,Fe)OOH at high pressures. *American Mineralogist* **104**, 1273-1284 (2019). https://doi.org/10.2138/am-2019-6913
24. X. Su *et al.*, Spectroscopic evidence for the Fe^{3+} spin transition in iron-bearing δ-AlOOH at high pressure. *American Mineralogist* **106**, 1709-1716 (2021). https://doi.org/10.2138/am-2021-7541
25. B. Strozewski *et al.*, Equation of state and spin crossover of (Al, Fe)-phase H. *Journal of Geophysical Research: Solid Earth* **128**, e2022JB026291 (2023). https://doi.org/10.1029/2022jb026291
26. M. Nishi *et al.*, Solid solution and compression behavior of hydroxides in the lower mantle. *Journal of Geophysical Research: Solid Earth* **124**, 10231-10239 (2019). https://doi.org/10.1029/2019jb018146
27. N. Bolfan-Casanova, H. Keppler, D. C. Rubie, Water partitioning between nominally anhydrous minerals in the MgO–SiO_2–H_2O system up to 24 GPa: implications for the distribution of water in the Earth's mantle. *Earth and Planetary Science Letters* **182**, 209-221 (2000). https://doi.org/10.1016/S0012-821X(00)00244-2
28. N. Bolfan-Casanova, S. Mackwell, H. Keppler, C. McCammon, D. C. Rubie, Pressure dependence of H solubility in magnesiowüstite up to 25 GPa: Implications for the

storage of water in the Earth's lower mantle. *Geophysical Research Letters* **29**, 89-81-89-84 (2002). https://doi.org/10.1029/2001gl014457

29. N. Bolfan-Casanova, H. Keppler, D. C. Rubie, Water partitioning at 660 km depth and evidence for very low water solubility in magnesium silicate perovskite. *Geophysical Research Letters* **30**, 1905 (2003). https://doi.org/10.1029/2003gl017182
30. Z. Liu *et al.*, Bridgmanite is nearly dry at the top of the lower mantle. *Earth and Planetary Science Letters* **570**, 117088 (2021). https://doi.org/10.1016/j.epsl.2021.117088
31. A. Sano-Furukawa *et al.*, Change in compressibility of δ-AlOOH and δ-AlOOD at high pressure: A study of isotope effect and hydrogen-bond symmetrization. *American Mineralogist* **94**, 1255-1261 (2009). https://doi.org/10.2138/am.2009.3109
32. J. Buchen, Seismic wave velocities in Earth's mantle from mineral elasticity. In *Mantle Convection and Surface Expressions,* H. Marquardt, M. Ballmer, S. Cottaar, J. Konter, Eds. (American Geophysical Union, Washington, D.C., 2021), pp. 51-95. https://doi.org/10.1002/9781119528609.ch3
33. I. Ohira *et al.*, The influence of δ-(Al,Fe)OOH on seismic heterogeneities in Earth's lower mantle. *Scientific Reports* **11**, 12036 (2021). https://doi.org/10.1038/s41598-021-91180-9
34. L. Stixrude, C. Lithgow-Bertelloni, Thermodynamics of mantle minerals - I. Physical properties. *Geophysical Journal International* **162**, 610-632 (2005). https://doi.org/10.1111/j.1365-246X.2005.02642.x
35. T. Ishii *et al.*, High pressure-temperature phase relations of basaltic crust up to mid-mantle conditions. *Earth and Planetary Science Letters* **584**, 117472 (2022). https://doi.org/10.1016/j.epsl.2022.117472
36. T. Irifune *et al.*, Iron partitioning and density changes of pyrolite in Earth's lower mantle. *Science* **327**, 193-195 (2010). https://doi.org/10.1126/science.1181443
37. D. J. Frost *et al.*, Experimental evidence for the existence of iron-rich metal in the Earth's lower mantle. *Nature* **428**, 409-412 (2004). https://doi.org/10.1038/nature02413
38. H. Hsu, Y. G. Yu, R. M. Wentzcovitch, Spin crossover of iron in aluminous $MgSiO_3$ perovskite and post-perovskite. *Earth and Planetary Science Letters* **359-360**, 34-39 (2012). https://doi.org/10.1016/j.epsl.2012.09.029
39. K. Glazyrin *et al.*, Magnesium silicate perovskite and effect of iron oxidation state on its bulk sound velocity at the conditions of the lower mantle. *Earth and Planetary Science Letters* **393**, 182-186 (2014). https://doi.org/10.1016/j.epsl.2014.01.056
40. J. F. Lin *et al.*, High-spin Fe^{2+} and Fe^{3+} in single-crystal aluminous bridgmanite in the lower mantle. *Geophysical Research Letters* **43**, 6952-6959 (2016). https://doi.org/10.1002/2016gl069836
41. R. Nomura *et al.*, Low core-mantle boundary temperature inferred from the solidus of pyrolite. *Science* **343**, 522-525 (2014). https://doi.org/10.1126/science.1248186
42. G. Fiquet *et al.*, Melting of peridotite to 140 gigapascals. *Science* **329**, 1516-1518 (2010). https://doi.org/10.1126/science.1192448
43. H. Piet *et al.*, Spin and valence dependence of iron partitioning in Earth's deep mantle. *Proceedings of the National Academy of Sciences U.S.A.* **113**, 11127-11130 (2016). https://doi.org/10.1073/pnas.1605290113
44. J. M. Jackson *et al.*, A synchrotron Mössbauer spectroscopy study of $(Mg,Fe)SiO_3$ perovskite up to 120 GPa. *American Mineralogist* **90**, 199-205 (2005). https://doi.org/10.2138/am.2005.1633

45. Y.-Y. Chang *et al.*, Spin transition of Fe^{3+} in Al-bearing phase D: An alternative explanation for small-scale seismic scatterers in the mid-lower mantle. *Earth and Planetary Science Letters* **382**, 1-9 (2013). https://doi.org/10.1016/j.epsl.2013.08.038
46. X. Wu *et al.*, Two-stage spin transition of iron in FeAl-bearing phase D at lower mantle. *Journal of Geophysical Research: Solid Earth* **121**, 6411-6420 (2016). https://doi.org/10.1002/2016jb013209
47. Y. Miyazaki, J. Korenaga, A wet heterogeneous mantle creates a habitable world in the Hadean. *Nature* **603**, 86-90 (2022). https://doi.org/10.1038/s41586-021-04371-9
48. E. J. Garnero, A. K. McNamara, S.-H. Shim, Continent-sized anomalous zones with low seismic velocity at the base of Earth's mantle. *Nature Geoscience* **9**, 481-489 (2016). https://doi.org/10.1038/ngeo2733
49. A. K. McNamara, A review of large low shear velocity provinces and ultra low velocity zones. *Tectonophysics* **760**, 199-220 (2019). https://doi.org/10.1016/j.tecto.2018.04.015
50. V. H. Lai *et al.*, Strong ULVZ and slab interaction at the northeastern edge of the Pacific LLSVP favors plume generation. *Geochemistry, Geophysics, Geosystems* **23**, e2021GC010020 (2022). https://doi.org/10.1029/2021gc010020
51. T. Kawazoe *et al.*, Single crystal synthesis of δ-(Al,Fe)OOH. *American Mineralogist* **102**, 1953-1956 (2017). https://doi.org/10.2138/am-2017-6153
52. J. Buchen, W. Sturhahn, T. Ishii, J. M. Jackson, Vibrational anisotropy of δ-(Al,Fe)OOH single crystals as probed by nuclear resonant inelastic X-ray scattering. *European Journal of Mineralogy* **33**, 485-502 (2021). https://doi.org/10.5194/ejm-33-485-2021
53. Y. Fei *et al.*, Toward an internally consistent pressure scale. *Proceedings of the National Academy of Sciences U.S.A.* **104**, 9182-9186 (2007). https://doi.org/10.1073/pnas.0609013104
54. A. Dewaele, M. Torrent, P. Loubeyre, M. Mezouar, Compression curves of transition metals in the Mbar range: Experiments and projector augmented-wave calculations. *Physical Review B* **78**, 104102 (2008). https://doi.org/10.1103/PhysRevB.78.104102
55. H. Liu *et al.*, Phase transition and compression behavior of gibbsite under high-pressure. *Physics and Chemistry of Minerals* **31**, 240-246 (2004). https://doi.org/10.1007/s00269-004-0390-2
56. N. Holtgrewe, E. Greenberg, C. Prescher, V. B. Prakapenka, A. F. Goncharov, Advanced integrated optical spectroscopy system for diamond anvil cell studies at GSECARS. *High Pressure Research* **39**, 457-470 (2019). https://doi.org/10.1080/08957959.2019.1647536
57. C. Prescher, T-Rax, version 1.1. *GitHub*, (2016). www.github.com/CPrescher/T-Rax
58. C. Prescher, V. B. Prakapenka, DIOPTAS: a program for reduction of two-dimensional X-ray diffraction data and data exploration. *High Pressure Research* **35**, 223-230 (2015). https://doi.org/10.1080/08957959.2015.1059835
59. C. Prescher, DIOPTAS, versions 0.5.0 to 0.5.2. *GitHub*, (2019-2020). www.github.com/Dioptas/Dioptas
60. W. Sturhahn, MINUTI, version 2.2.1. (2021). www.nrixs.com
61. J. Rodríguez-Carvajal, Recent advances in magnetic structure determination by neutron powder diffraction. *Physica B* **192**, 55-69 (1993). https://doi.org/10.1016/0921-4526(93)90108-I
62. J. Rodríguez-Carvajal, FullProf, version 2.6.2. (2020). www.ill.eu/sites/fullprof/index.html

63. Y. Akahama, H. Kawamura, Pressure calibration of diamond anvil Raman gauge to 310 GPa. *Journal of Applied Physics* **100**, 043516 (2006). https://doi.org/10.1063/1.2335683
64. T. S. Toellner, Monochromatization of synchrotron radiation for nuclear resonant scattering experiments. *Hyperfine Interactions* **125**, 3-28 (2000). https://doi.org/10.1023/A:1012621317798
65. W. Sturhahn, CONUSS and PHOENIX: Evaluation of nuclear resonant scattering data. *Hyperfine Interactions* **125**, 149-172 (2000). https://doi.org/10.1023/A:1012681503686
66. W. Sturhahn, PHOENIX, version 3.0.4. (2021). www.nrixs.com
67. W. Sturhahn, Nuclear resonant spectroscopy. *Journal of Physics: Condensed Matter* **16**, S497-S530 (2004). https://doi.org/10.1088/0953-8984/16/5/009
68. W. Sturhahn, V. G. Kohn, Theoretical aspects of incoherent nuclear resonant scattering. *Hyperfine Interactions* **123**, 367-399 (1999). https://doi.org/10.1023/A:1017071806895
69. Y. Tanabe, S. Sugano, On the absorption spectra of complex ions. I. *Journal of the Physical Society of Japan* **9**, 753-766 (1954). https://doi.org/10.1143/JPSJ.9.753
70. W. Sturhahn, J. M. Jackson, J.-F. Lin, The spin state of iron in minerals of Earth's lower mantle. *Geophysical Research Letters* **32**, L12307 (2005). https://doi.org/10.1029/2005gl022802
71. R. G. Burns, *Mineralogical Applications of Crystal Field Theory*. (Cambridge University Press, Cambridge, 1993). https://doi.org/10.1017/CBO9780511524899
72. J. Ita, L. Stixrude, Petrology, elasticity, and composition of the mantle transition zone. *Journal of Geophysical Research* **97**, 6849-6866 (1992). https://doi.org/10.1029/92JB00068
73. Z. Wu, J. F. Justo, C. R. S. da Silva, S. de Gironcoli, R. M. Wentzcovitch, Anomalous thermodynamic properties in ferropericlase throughout its spin crossover. *Physical Review B* **80**, 014409 (2009). https://doi.org/10.1103/PhysRevB.80.014409
74. L. Stixrude, C. Lithgow-Bertelloni, Thermodynamics of mantle minerals - II. Phase equilibria. *Geophysical Journal International* **184**, 1180-1213 (2011). https://doi.org/10.1111/j.1365-246X.2010.04890.x

Acknowledgments

J.B. was supported by National Science Foundation's (NSF) Collaborative Studies of the Earth's Deep Interior under EAR–1161046 and EAR–2009935 awarded to J.M.J. and through the project DEEP-MAPS funded by the European Research Council (ERC) and awarded to Hauke Marquardt (University of Oxford). This research used resources of the Advanced Photon Source (APS), a U.S. Department of Energy (DOE) Office of Science User Facility operated for the DOE Office of Science by Argonne National Laboratory under contract no. DE-AC02-06CH11357. Portions of this work were performed at GeoSoilEnviroCARS (The University of Chicago, Sector 13), Advanced Photon Source, Argonne National Laboratory.

GeoSoilEnviroCARS is supported by the National Science Foundation – Earth Sciences (EAR–1634415). Beamlines 3-ID-B and 13-ID-D at APS are partially supported by COMPRES, the Consortium for Materials Properties Research in Earth Sciences under NSF cooperative agreement EAR–1606856.

Author contributions

J.B. and J.M.J. designed the research project. J.B. prepared XRD and NRIXS experiments, analyzed experimental data, developed thermodynamic models, and wrote the manuscript. J.M.J. and W.S. validated data analyses. W.S. wrote and maintains the software MINUTI and PHOENIX. J.B., O.P., V.V.D., W.S., and J.M.J. performed XRD and NRIXS experiments. S.C., E.G., and T.S.T. assisted with experiments at APS. T.I. synthesized and characterized δ-$Al_{0.87}Fe_{0.13}OOH$ samples. All authors commented on the manuscript.

Competing interests

The authors declare that they have no competing interests.

Data and materials availability

All data needed to evaluate the conclusions in the paper are presented or cited in the paper and/or the Supplementary Materials. Supplementary Tables S1 and S2 are available from the corresponding author upon request.

Tables (see following pages)

952 **Table 1: Isothermal equation of state of δ-$Al_{0.87}Fe_{0.13}OOH$**

Isothermal contribution		
V_0	(Å^3)	56.93(4)
K_0	(GPa)	205(3)
K_0'		4.34(8)
Electronic contribution		
Δ_0	(cm^{-1})	15374(94)
B_0	(cm^{-1})	655*
B/C		4.73*
δ		5*
b	(= c)	–0.94(12)

The isothermal contribution is described by a 3rd order Birch-Murnaghan equation of state. The electronic contribution is described by a crystal-field model (*32*).

* values from (*71*)

953

954

955

956

957

958

959

960 **Table 2: Quasi-harmonic parameters of δ-$Al_{0.87}Fe_{0.13}OOH$**

		FeOOH component			AlOOH component	
		$^6A_1$	$^2T_2$	$^4T_1$	δ	δ-AlOOH
V_0	(Å^3)	*56.93*	*55.50*	*56.27*	*56.93*	*55.13*
θ_0	(K)	402(6)	336(12)	369(7)*	1357(883)	526(422)
γ_0		*1*	4.89(27)	2.95(14)*	1.24(37)	1.62(10)
q_0		*1*	*1*	*1*	2.05(1.07)	3.19(21)

Values in *italics* were fixed during fitting. The parameters for the FeOOH component were derived from high-pressure NRIXS data. The parameters for the AlOOH component (δ) were derived from high-pressure high-temperature XRD data. For comparison, the parameters for pure δ-AlOOH were derived by refitting previously reported data (*16*) to a Debye model (*34*).
* average of $^6A_1$ and $^2T_2$

961

962

963

964

965

966

967

968

969

970

971

972

Supplementary figures

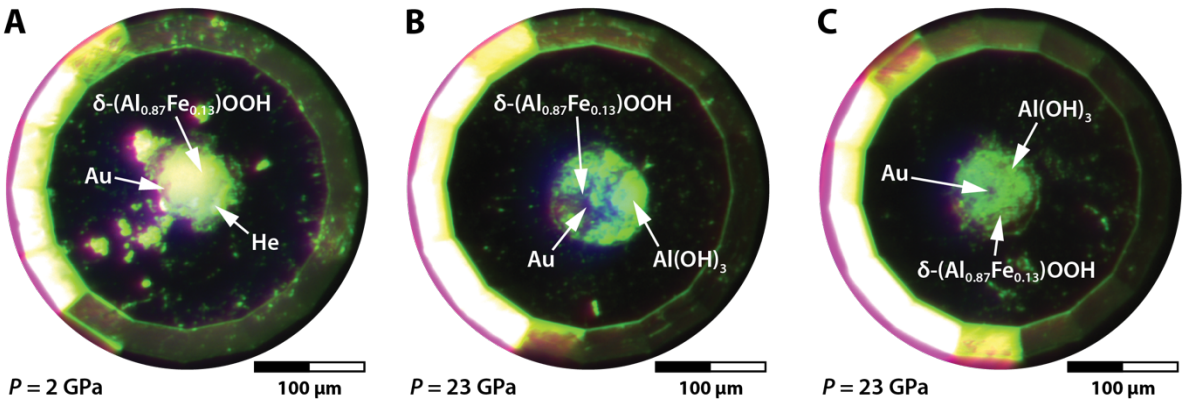

Fig. S1: Pressure chambers of diamond anvil cells for X-ray diffraction experiments. (**A**) For X-ray diffraction experiments at high pressures and room temperature, powder of δ-$Al_{0.87}Fe_{0.13}OOH$ was loaded together with gold (Au, pressure calibrant) and helium (He, pressure-transmitting medium). (**B**) For X-ray diffraction experiments at simultaneously high pressures and high temperatures, powder of δ-$Al_{0.87}Fe_{0.13}OOH$ and gold (Au, pressure calibrant) were embedded in $Al(OH)_3$, which served as pressure-transmitting medium and thermal insulation and prevented dehydration of δ-$Al_{0.87}Fe_{0.13}OOH$ during laser heating.

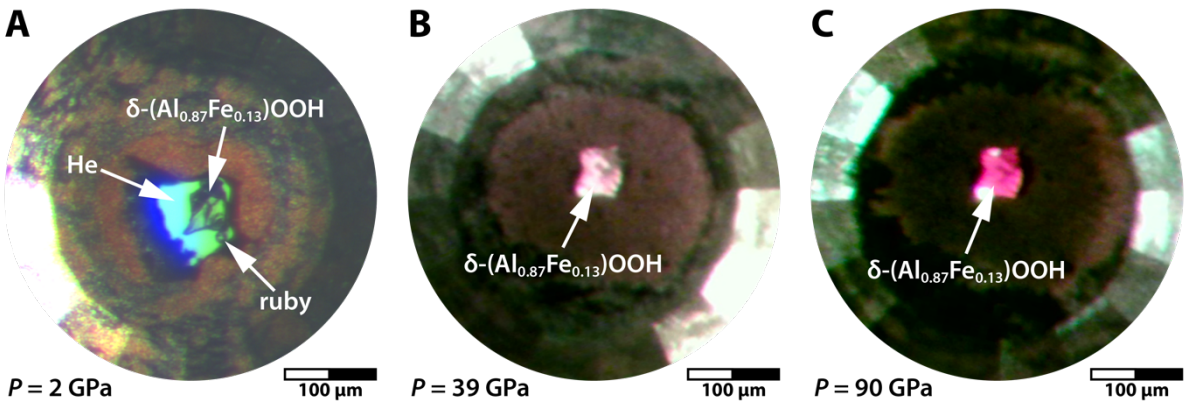

Fig. S2: Pressure chamber of the diamond anvil cell for nuclear resonant inelastic X-ray scattering experiments at different pressures. (**A**) 2 GPa. (**B**) 39 GPa. (**C**) 90 GPa. A grain of δ-$Al_{0.87}Fe_{0.13}OOH$ was loaded together with a ruby sphere (ruby, pressure calibrant) and helium (He, pressure-transmitting medium). With increasing pressure, the helium (partly) escaped from the pressure chamber. Note the change in color of δ-$Al_{0.87}Fe_{0.13}OOH$ from pale orange at low pressures to bright red at high pressures.

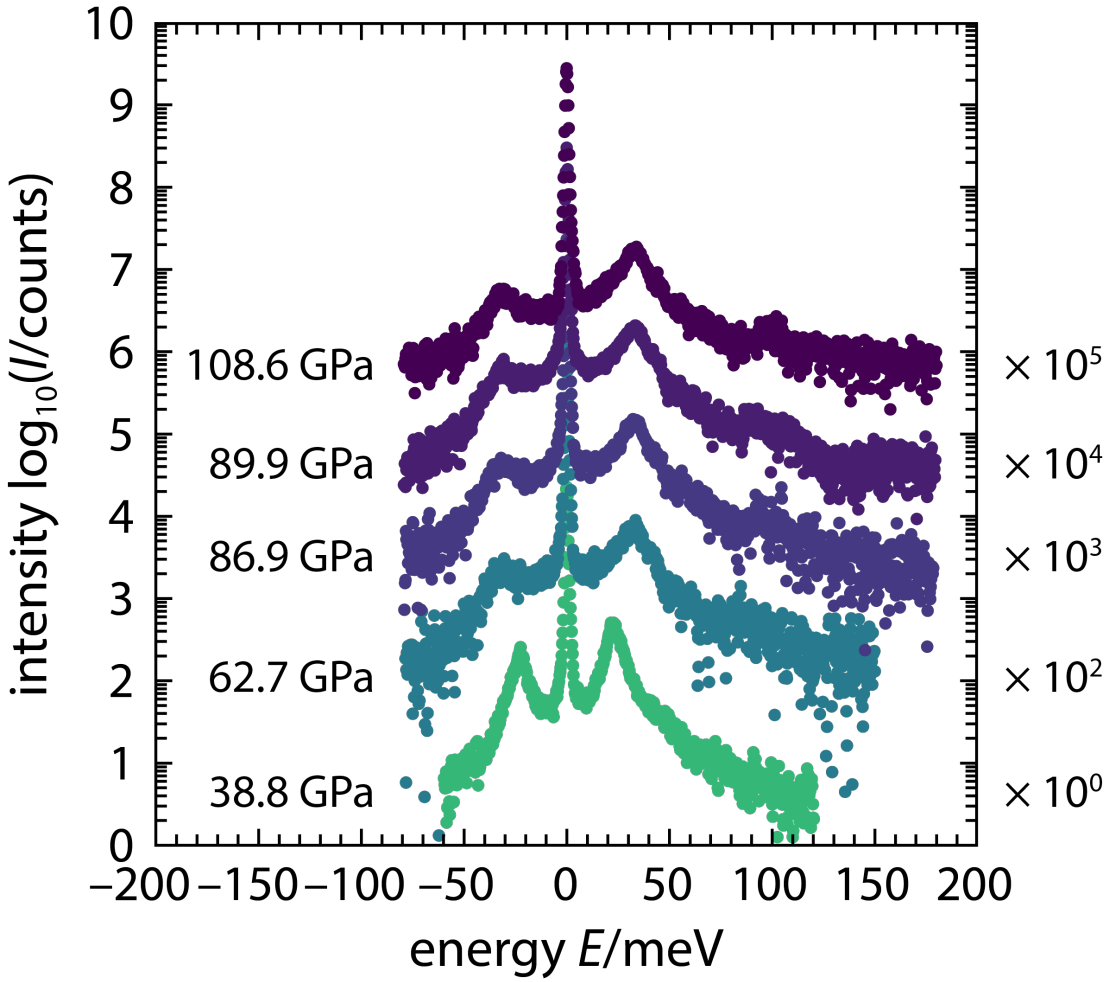

Fig. S3: High-pressure nuclear resonant inelastic X-ray scattering spectra. Nuclear resonant inelastic X-ray scattering (NRIXS) spectra of δ-$Al_{0.87}Fe_{0.13}OOH$ with $^{57}Fe/\Sigma Fe$ = 96 % recorded at different pressures and room temperature. Spectra are vertically offset for clarity as indicated on the right.